Marine Geology 439 (2021) 106564

Contents lists available at ScienceDirect

Marine Geology

journal homepage: www.elsevier.com/locate/margo

Post-LGM multi-proxy sedimentary record of bottom-current variability and downslope sedimentary processes in a contourite drift of the Gela Basin (Strait of Sicily)

Tugdual Gauchery [a,b], Marzia Rovere [a,*], Claudio Pellegrini [a], Alessandra Asioli [a], Tommaso Tesi [c], Antonio Cattaneo [d], Fabio Trincardi [a]

[a] Istituto di Scienze Marine (ISMAR), Consiglio Nazionale delle Ricerche, via Gobetti 101, 40129 Bologna, Italy
[b] Dipartimento di Ingegneria Civile, Chimica, Ambientale e dei Materiali, Viale del Risorgimento 2, 40136 Bologna, Italy
[c] Istituto di Scienze Polari, Consiglio Nazionale delle Ricerche, via Gobetti 101, 40129 Bologna, Italy
[d] Institut français de recherche pour l'exploitation de la mer (Ifremer), Géosciences Marines, Z.I Pointe du Diable, BP70 Plouzané, France

ARTICLE INFO

Editor: Michele Rebesco

Keywords:
Mediterranean oceanography
Gela Basin
Contourite drifts
Mass-transport deposits
Sedimentary facies
Sortable silt
Bioecozone
Post-LGM
Ichnofacies

ABSTRACT

Depositional systems accumulating under the combined influence of along-slope currents and downslope sediment-gravity flows are frequent in several continental margins. Despite being well-documented in terms of how these opposing depositional processes shape the margin architecture, many aspects related to their interaction and distinctive characters of resulting sediment accumulations remain elusive. Here we focus on the Gela Basin, the foredeep of the Maghrebian fold-and-thrust belt in the Strait of Sicily, where the Levantine Intermediate Water (LIW) and the Modified Atlantic Water (MAW) are confined by margin morphology, which amplify their velocities. Two sediment cores located on the upper and lower slope of the Gela Basin document the overlapping of along- and downslope processes since the very last phase of the Last Glacial Maximum (LGM). Detailed analysis of several proxies including sedimentary structures, sortable silt, geochemical elemental composition, oxygen and carbon isotopes, ichnofacies and foraminifera assemblages helped to disentangle the sedimentary imprints of contourites (including variations in bottom-current velocity through time) and downslope gravity-driven processes (turbidity currents and mass-transport processes).

The slope experienced exceptionally high sedimentation rates up to 1300 cm kyr^{-1} during the last phase of LGM and early phase of Heinrich Stadial 1 (HS1), which rapidly decreased before Heinrich Event 1 (< 100 cm kyr^{-1}). The high accumulation rates were driven by a combination of sediment input from the inner and mid shelf and lateral advection promoted by strong bottom-currents under the action of the LIW. An abrupt and brief intensification (+ 7.8 cm^{-1}) of the MAW speed during the early phase of HS1 affected the stability of the sediment drifts, which were growing since the previous interglacial and contributed to the emplacement of mass-transport deposits around 17 kyr BP. During the post-glacial sea-level rise pulses, before and during the Heinrich Event 1, the two sediment cores registered contrasting bottom-current velocities, suggesting a progressive shoaling of the LIW and modifications at the interface between the LIW and the MAW, in response to the increased fresh water discharge from the Atlantic. Our findings suggest that sea-level fluctuations can change the thickness and core-depth of the Central Mediterranean water masses, leading to intervals of enhanced bottom-current erosion and margin instability along the outer shelf and upper slope.

1. Introduction

Contourite deposits are considered excellent archives for reconstructing paleoceanographic circulation at regional scale as a key aspect of climatic variability (e.g., Hernandez-Molina et al., 2014). Furthermore, numerous studies use their sedimentary record to reconstruct variations in bottom-current flow strength through time (McCave et al., 1995; Toucanne et al., 2012; Miramontes et al., 2016). Bottom currents can be in fact governed by geostrophic thermohaline circulation and occur with variable intensities that directly influence their

* Corresponding author.
E-mail address: m.rovere@ismar.cnr.it (M. Rovere).

https://doi.org/10.1016/j.margeo.2021.106564
Received 5 February 2021; Received in revised form 28 June 2021; Accepted 4 July 2021
Available online 10 July 2021

ability for inducing lateral advection of sediment (Rebesco et al., 2014; Pellegrini et al., 2016). The signature of contour-currents is relatively well-preserved where current intensity is high and in areas where seafloor morphology generates lateral flow constriction and this often happens in the upper slope around headlands, volcanic islands, submarine plateaus (Van Rooij et al., 2010; Martorelli et al., 2011; Rovere et al., 2019).

Along-slope contour currents often occur on continental margins where also downslope gravity flows are common. Interactions between contour currents and gravity flows are rarely documented, especially at the sedimentary and seismic facies level, either because the criteria to identify them are sometimes ambiguous in interbedded sedimentary sequences (e.g. Stow and Smillie, 2020) or because gravity flows usually overprint bottom-current sedimentary structures (Mulder et al., 2008). On the other hand, contour currents may in part obliterate sedimentary structures related to turbidity-current deposition through the winnowing of fine grains (e.g. Martín-Chivelet et al., 2008). Therefore, from a sedimentary standpoint, in dynamic environments where along- and downslope processes occur simultaneously during strata deposition, it remains crucial to find diagnostic tools to disentangle strata recording bottom-current activity from strata emplaced by downslope gravity-driven processes (e.g. landslides, turbidity currents, wave-enhanced sediment gravity flows).

Several continental margins dominated by the Atlantic-Mediterranean thermohaline circulation show the interplay between along-slope and downslope processes and have been investigated at the sedimentary body level (Brackenridge et al., 2013; Martorelli et al., 2016; Miramontes et al., 2016), in flume tank experiments (Miramontes et al., 2020), but to a lesser extent at the sedimentary facies level (Beckers et al., 2016). Shallow- and intermediate-water contourites can more frequently record the interplay with gravity flows process, especially during sea-level lowstands when sediment flux from land and downslope transport are usually enhanced (Lee, 2009). In addition, the upper continental slope and shelf-edge areas are directly affected by sea-level fluctuations, as the depth range of the wind-driven surface and intermediate water masses may change as well as their ability to impinge on the sea floor (Miramontes et al., 2016). However, only a minor set of studies focus on the small-scale dynamics of locally confined contourite drifts that develop in response to oceanographic changes such as the lateral shift and vertical migration of water masses (e.g. Hanebuth et al., 2015; Petrovic et al., 2019).

In the Mediterranean Sea, the Strait of Sicily is a relatively-shallow sill separating the much deeper western and eastern basins and represents a 2-layer gateway for Atlantic and Eastern Mediterranean water exchange, where surface and intermediate currents are recorded (Béranger et al., 2004). In the Strait of Sicily, several confined shallow-water contourite deposits have been identified on the shelf and upper slope of the Gela Basin (Verdicchio and Trincardi, 2008; Kuhlmann et al., 2015; Gauchery et al., 2021). Contourites mainly formed by the action of the Levantine Intermediate Water (LIW) during interglacials and sea-level highstands when the intensity of the flow is believed to increase along the eastern slope of the Gela Basin. Contourites forming on the outer shelf are controlled by the displacing action of the Mediterranean Surface Water (MAW) (Gauchery et al., 2021). The presence of rapidly deposited contourite drift deposits in the upper slope that concurred to high sediment accumulation rates (250–330 cm/kyr) since the Last Glacial Maximum (LGM, ~ 19–23 ka) are considered the main factors conducive to recurrent slope failure with the emplacement of several mass-transport deposits (MTDs) in the northern Gela Basin (Minisini and Trincardi, 2009).

This paper presents paleo archives of post-LGM from two sediment piston cores collected in the upper and lower slope of the southern Gela Basin along a sediment drift and downslope of two MTDs, generated by the collapse of the sediment drift itself. Our multi-proxy approach includes seismic stratigraphy, benthic and planktonic foraminifera assemblages, stable isotope geochemistry, geochemical element ratios, sortable silt grain size to distinguish between strata recording bottom-current activity alone and in combination with other sedimentary processes (e.g. gravity-driven flows). Diagnostic radiographic images of sedimentary structures were integrated with the carbon isotopic fingerprint of plant debris and displaced foraminifera from the shelf to infer the occurrence of downslope transport. The ichnofacies of bioturbating fauna was analysed to understand bottom oxygen conditions and infer proximity to the bottom-current core.

By reconstructing the depositional history of two sedimentary records of the Gela Basin, this paper aims to: 1) evaluate proxies and criteria to disentangling along- vs downslope processes; 2) reconstruct bottom-current activity during the post-LGM, with particular focus on the stratigraphically-expanded Heinrich Stadial 1; 3) discuss time intervals and predisposing conditions that lead to the failure of sectors of the sediment drifts. Overall, the climatic signal stored in the sedimentary records in the form of variability of the paleo-current activity and intensity enabled us to make inferences on the general Mediterranean circulation, with reference to the post-LGM sea-level fluctuations.

2. Background

2.1. Geological setting

The Gela Basin is located in the Strait of Sicily and represents the foredeep of the Maghrebian fold-and-thrust belt, is shaped by the most recent arcuate front of the Gela Nappe in the north (Argnani, 1987) and constrained by the 100–150 m deep Malta Plateau in the east (Fig. 1A). The basin reaches the maximum water depth (wd) of 936 m and is filled by turbidites, mass-transport (MTD) and contourite deposits of Pliocene-Quaternary age overlying Messinian evaporites and fine-grained marls of the early Pliocene Trubi Formation. Sediments are represented by clays intercalated with thin-bedded fine-grained sands in distal settings and thicker sand beds on the southern Sicily slope (Ghielmi et al., 2012).

Sedimentary prograding wedges, fed from the north, developed on top of the Gela Nappe starting from the late Pliocene and extended eastward, away from the thrust front, fringing the Hyblean Plateau (Fig. 1B). In the Pleistocene, progradation extended to the south of the basin with the emplacement of oblique shelf-edge clinothems (Gauchery et al., 2021). From Pliocene to the Middle Pleistocene Transition (ca. 800 ka), the sediment wedge increased in thickness by 150 m/Myr. In the last 800 kyr, the margin outbuilding developed a markedly aggradational motif, with sediment accumulation rate reaching 900 m/Myr, suggesting an overall increase in accommodation on the continental shelf accompanied by an increased sediment flux along the eastern margin of the Gela Basin (Gauchery et al., 2021).

Sedimentation rates as low as 11 cm/kyr have been observed for the last 30 kyr BP in the western Gela Basin at ODP site 963 (Shipboard Scientific Party, 1996). On the contrary, sediment cores document accumulation rates up to 200 cm/kyr during the last major interglacial period before the Holocene (MIS 5, 120 to 70 ka) and 100 cm/kyr in the last 18 kyr BP (Kuhlmann et al., 2015) in the eastern Gela Basin. To explain particularly high sedimentation rates during MIS 5 Interglacials and short-lived relative high stands, Kuhlmann et al. (2015) hypothesized the action of intermittent hyperpycnal flows acting during overall arid climate in addition to enhanced thermohaline circulation. The hydrological regime of Sicilian rivers still reflects one of the most arid conditions in the Mediterranean with a discharge of Gela River as low as 0.02 km^3/yr (Milliman and Farnsworth, 2011; Fig. 1C).

2.2. Oceanographic regime since Last Glacial Maximum

The Mediterranean Sea is connected with the Atlantic Ocean via the Strait of Gibraltar where the relatively fresher and warmer ocean waters enter and transform into the Modified Atlantic Water (MAW) (Astraldi et al., 1999). The MAW flows eastward onto the Eastern Mediterranean via the Strait of Sicily with a velocity of 15–30 cm s^{-1} between 100 and

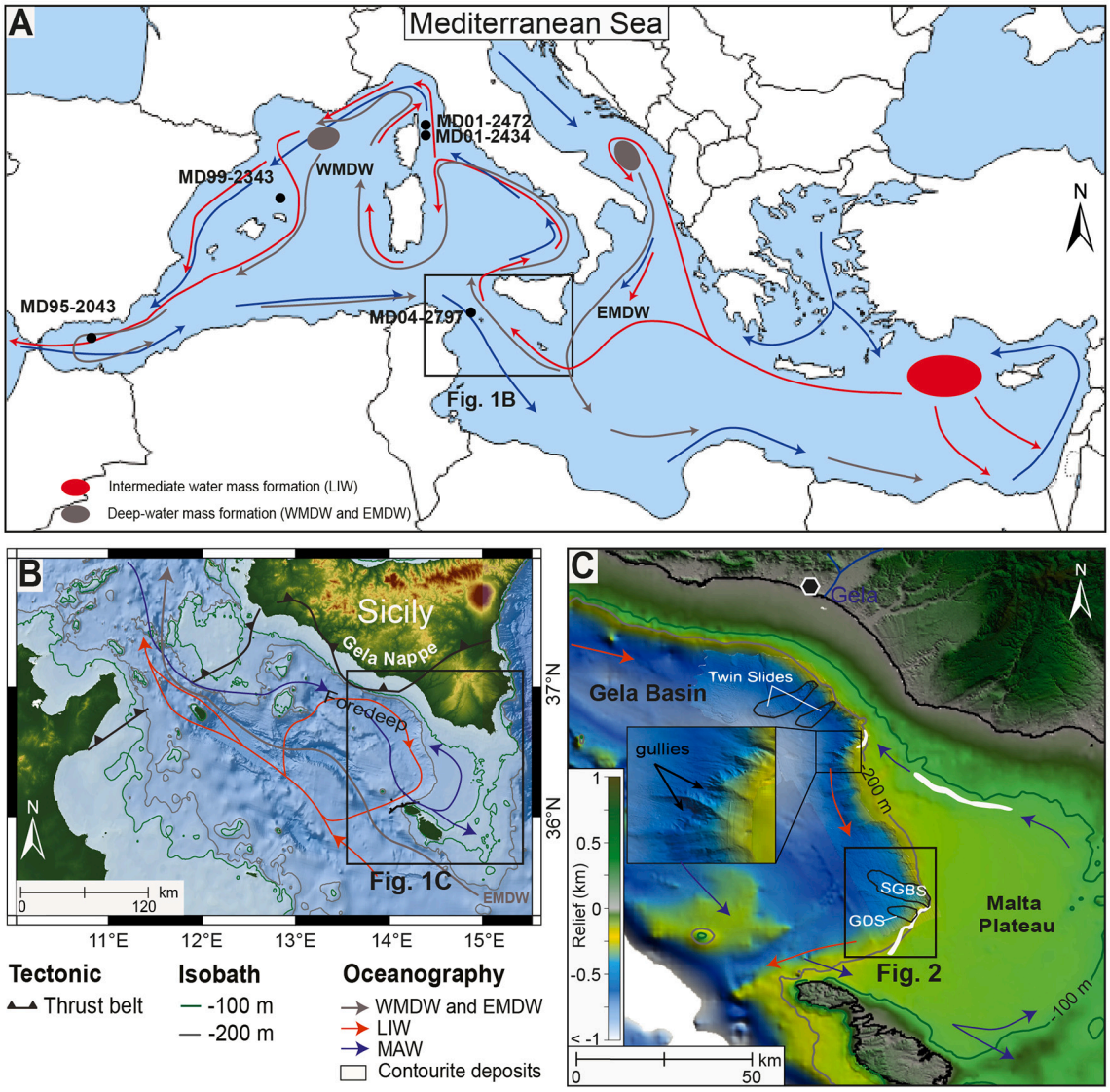

Fig. 1. A) Circulation of the surface (Modified Atlantic Water – MAW), intermediate (Levantine Intermediate Water – LIW) and deep-waters (Western and Eastern Mediterranean Deep Water – WMDP and EMDW) in the Mediterranean Sea (modified from Astraldi et al., 2001). The black circles indicate the location of the reference cores used in this study. B) Relief and bathymetric map of the Strait of Sicily area with superimposed the water mass circulation and the general tectonic framework (modified from Millot, 1999; Millot and Taupier-Letage, 2005). C) Relief and bathymetric map of the Gela Basin highlighting mass-transport deposits: Twin Slides (Minisini et al., 2007), Southern Gela Basin Slide (SGBS) and Gela Drift Slide (GDS) (Gauchery et al., 2021). White polygons indicate contourite deposits (Verdicchio and Trincardi, 2008; Gauchery et al., 2021).

200 m wd (Lermusiaux and Robinson, 2001; Millot and Taupier-Letage, 2005; Fig. 1A). The increasing evaporation and temperature from west to east promote vertical mixing during wintertime and result in the formation of the Levantine Intermediate Water (LIW) in the Levantine Basin (Millot and Taupier-Letage, 2005; Fig. 1A). The LIW flows westward via the Strait of Sicily during summer with a velocity of 13 cm s^{-1} between 200 and 600 m wd (Fig. 1B; Lermusiaux and Robinson, 2001; Sammari et al., 1999). Both LIW and MAW have likely been active through the Quaternary but experienced variations in flow direction and velocity with sea-level fluctuations (Gauchery et al., 2021). Deep waters form in the Mediterranean due to mixing of cooled surface winter waters and the LIW in the northern Adriatic Sea (Eastern Mediterranean Deep Water; Astraldi et al., 2001) and in the Gulf of Lions (Western Mediterranean Deep Water; Millot, 1999) (Fig. 1A).

During the LGM, sea level was ~135 m below the modern position (Lambeck et al., 2014) and the limited amount of freshwater input through the reduced section of the Gibraltar Gateway contributed to intensify intermediate and deep-water formation, resulting in stronger bottom currents in the Mediterranean Sea (Rogerson et al., 2008; Toucanne et al., 2012; Miramontes et al., 2016). Well-mixed and ventilated water masses persisted during Greenland Stadial GS-2a even when massive iceberg melting at the Heinrich Event 1 (HE1) considerably reduced the salinity of the surface Mediterranean waters and caused profound reduction of deep-water formation and thermohaline circulation (Sierro et al., 2005). Indeed, during HE1 strong LIW dynamics characterized the Western (Jiménez-Espejo et al., 2015) and Central Mediterranean (Toucanne et al., 2012), while circulation was sluggish in the Eastern Mediterranean mostly due to reduced water exchange across the Strait of Sicily (Cornuault et al., 2018).

At the last glacial/interglacial transition during Greenland Interstadial 1 (GI-1) about 15 ka, a drastic reduction of the ventilation and velocity of the LIW was documented in the Corsica Trough (Toucanne et al., 2012), coinciding with warmer climate (i.e. Bølling-Allerød period) and large eustatic sea-level rise (i.e. Meltwater Pulse 1A, Deschamps et al., 2012). Moreover, the onset of the African Humid Period (AHP) at 14.8 kyr BP, when gradually increasing Northern

Hemisphere summer insolation drove the intensification and northward migration of the African monsoon (see Shanahan et al., 2015 and references therein), promoted continental runoff from North Africa into the Mediterranean Sea (see Rohling et al., 2015 for a complete review). The excess of freshwater input during pluvial maxima of the AHP acted as an additional forcing to the system and drastically changed the circulation pattern in the Central and Eastern Mediterranean (Toucanne et al., 2012; Revel et al., 2015), probably through a partial inhibition of the vertical mixing (Schmiedl et al., 2010).

The intense and short cooling period known as Greenland Stadial 1 (GS-1) was characterized by a decrease in the Atlantic surface temperatures and salinity depletion due to fast southward shift of the polar front (Cacho et al., 2001). In the Mediterranean Sea, the arid climatic conditions favoured a more intense LIW circulation associated with lower oxygenation and higher productivity (Toucanne et al., 2012; Jiménez-Espejo et al., 2015).

The transition to warmer conditions (10.8 to 6.8 ka, Cacho et al., 2001), coupled with enhanced Nile runoff, which led to deposition of Sapropel S1 (Rohling et al., 2015), significantly slowed down the LIW dynamics in the Western (Jiménez-Espejo et al., 2015; Dubois-Dauphin et al., 2017) and Eastern Mediterranean (Toucanne et al., 2012; Tesi et al., 2017), with reduced water exchange at the Strait of Sicily (Cornuault et al., 2018).

2.3. Contourite-derived mass-transport deposits

Contourite deposits are widespread along the shelf-edge and upper slope (~ 200 m wd) of the northern (Verdicchio and Trincardi, 2008) and southern (Gauchery et al., 2021) Gela Basin as well as over the shallow-water area of the Malta Plateau (~135 m wd, Fig. 1C) south of Sicily (Gauchery et al., 2021). Given the water depth of their occurrence, these contourite deposits reflect the action of intermediate waters (LIW, Verdicchio and Trincardi, 2008) and surface circulation (MAW, Gauchery et al., 2021).

In the northern Gela Basin multi-stage and stacked mass-transport deposits (MTDs) have been recorded since 87 kyr BP with ~10 kyr return frequency and involve contourites and clinothem deposits (Kuhlmann et al., 2017). During LGM, small-scale landslide deposits that are not discernible in seismic reflection profiles are revealed by the presence of displaced foraminifera (Kuhlmann et al., 2017). The uppermost of these minor stacked mudflow deposits occurred about 8.5 kyr BP and displaced the postglacial rapidly deposited units of the sediment drifts (Minisini and Trincardi, 2009). On top of the mudflow, the Twin Slides (Minisini et al., 2007) are the youngest MTD in the region and occurred in the late Holocene (Fig. 1C).

The contourite deposits located in the upper slope of the southern Gela Basin are composed of fine-grained sediment with well-developed sediment drifts and moats and their most recent phase of growth occurred during MIS 5 and late MIS 2 (Gauchery et al., 2021). The presence of erosional surfaces downcutting the upper slope combined with oversteepening caused by high sediment accumulation rates favoured the emplacement of the South Gela Basin Slide (SGBS) and the Gela Drift Slide (GDS). These two events reflect changes in sediment supply and dispersal by bottom-currents mainly due to sea-level fluctuations orbitally-controlled by climatic cycles paced at 100 kyr (Gauchery et al., 2021; Fig. 1C).

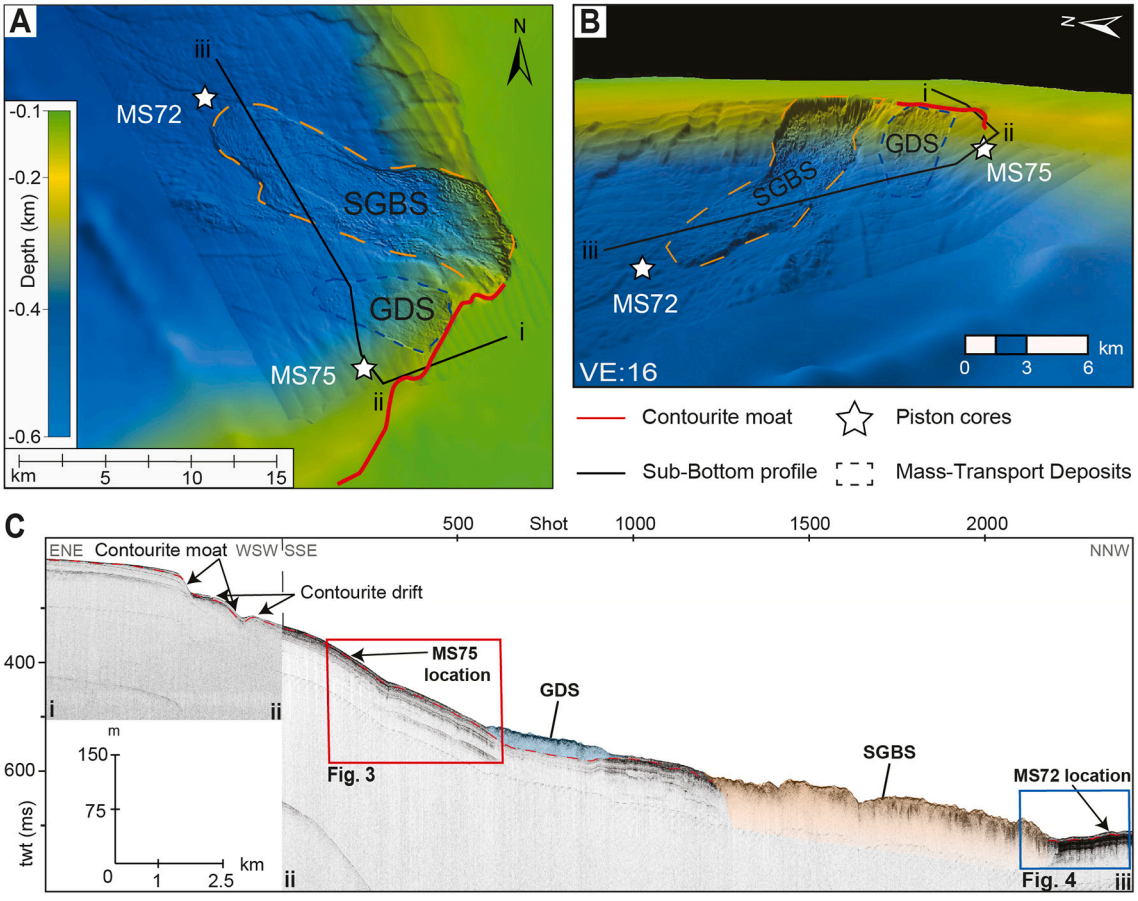

Fig. 2. A) 2D and B) 3D bathymetric map with location of cores MS75 and MS72 (white stars). The black line indicates the sub-bottom seismic reflection profile shown in C; the red line outlines a contour-parallel moat located upslope of the mass-transport deposits Southern Gela Basin Slide (SGBS) and Gela Drift Slide (GDS). C) Sub-bottom seismic reflection profile showing the location of cores MS75 and MS72. (For interpretation of the references to colour in this figure legend, the reader is referred to the web version of this article.)

3. Materials, methods and approach

3.1. Methods

3.1.1. Hydroacoustic data

Bathymetric maps were obtained from a compilation of a 1/16 × 1/16 arc minutes resolution EMODnet (EMODnet Bathymetry Consortium, 2016) with swath bathymetry data collected with a 50 kHz Reson Seabat® 8160 on board RV Urania in 2006 during the CORSARO survey (Fig. 2).

The sub-bottom seismic reflection profiles (Fig. 2C) were collected using a Teledyne Benthos CHIRP-III system on board RV Urania in 2006 during the MAKROS campaign. The transducer is composed of a 16 hull-mounted array with a sweep-modulated frequency of 2–20 kHz outgoing signal and 4 kW power per-channel enabling a vertical resolution of 0.5 m and shallow penetration (< 100 m).

3.1.2. Sediment cores

Two sediment cores were recovered using a piston corer on board RV Urania in 2007 during the MARCOS cruise (Fig. 2). Core MS75 was collected on the upper slope at 280 m water depth (wd) and is 842.5 cm long (Fig. 3); core MS72 was retrieved at 550 m wd in the lower slope and is 1078.5 cm long (Fig. 4). For stratigraphic correlations, additional reference from long piston cores were used from the literature (Fig. 1A for location).

3.2. Laboratory Analysis on sediment cores

X-ray images of the sediment cores were obtained with a Fuji PRIMA T2 digital acquisition system from Ibis X-rays systems and a Gilardoni cpx-m 160 generator. Magnetic susceptibility was acquired with a Bartington® system mounting an MS2 sensor (range 0.1 SI) and using a 2 cm spacing resolution.

X-ray fluorescence (XRF) data were acquired with a 3rd generation AVAATECH core scanner on split cores equilibrated for room temperature, carefully smoothened to remove surface roughness and covered with a 4 μm Ultralene® film to prevent contamination of the sensor during core logging. The generator is an Oxford 100-W X-Ray source with rhodium anode, while the sensor is a Canberra Silicon Drift Detector with Be window. The XRF data were collected in three separate runs using generator settings: 10 kV with helium flux, 30 kV, 50 kV and 400–450 μA with counting times of 10–35 s every centimetre downcore. Dead times were automatically corrected. Raw spectroscopic data were processed and converted to elemental counts by Iterative Least square software (WIN AXIL) package from Canberra Eurisys. Post-processing of the results indicated that light elements (Al to Fe) were affected by seawater content, with Cl values showing an opposite trend. Thus, light elements from lithogenic sources were replaced by heavier elements when normalizing XRF data (e.g. Fe replaced by Ti) (Hennekam and De Lange, 2012; Tjallingii et al., 2007).

Foraminifera assemblages were examined by means of an optical stereomicroscope to obtain a semi-quantitative micropaleontological analysis on 1 cm thick sediment slices taken every ~10 cm. The sediment samples were dried in oven at 50 °C and sieved at 0.063 mm in advance of the micropaleontology analysis.

Radiocarbon AMS dating were performed on monospecific samples (Table 1), when possible, of planktonic or benthonic foraminifera at the National Ocean Sciences Accelerator Mass Spectrometry Facility (NOSAMS, Woods Hole Oceanographic Institution, USA). Specimens were picked-up under the optical stereomicroscope from the size fraction >0.180 mm, discarding filled, encrusted and broken specimens. The selected specimens underwent an ultrasonic bath in demineralized water before shipping to the laboratory. The calibration was obtained with the Calib 7.1.0 Radiocarbon Calibration Program (Stuiver and Reimer, 1993) and the Marine13 calibration data set (Reimer et al., 2013) applying a reservoir age of 71 ± 50 years according to the Calib database for Sicily (Kuhlmann et al., 2015; Siani et al., 2000; Table 1).

Oxygen and carbon stable isotope analyses of foraminifera ($\delta^{13}C_{for\text{-}ams}$) were performed on the planktonic species *Globigerina bulloides* for both cores and on the benthonic taxon *Bulimina marginata* only for core MS72. These two taxa were selected because of their continuous presence in the cores and because they allow a comparison with other Mediterranean records. *G. bulloides* occurs in the Mediterranean Sea, preferentially in the western basin, during winter at water depth 50–200 m (Pujol and Vergnaud-Grazzini, 1995). Twenty-five specimens, where available, were picked-up for both taxa from the size fraction >0.180 mm and they were selected under the optical stereomicroscope to avoid broken, filled or encrusted specimens. The measurements were performed at the Leibniz Laboratory for Radiometric Dating and Stable Isotope Research, University of Kiel, Germany. The analytical precision is < ± 0.05‰ (^{13}C) and < ± 0.08‰ (^{18}O). The isotopic composition is reported as per mil (‰) deviation with respect to the Vienna Pee Dee Belemnite (VPDB) standard. The data were not corrected for the ice volume effect.

Plant debris was handpicked from the sieved sediment and transferred in silver cups, where samples were acidified with 1.5 M HCl twice. Elemental (organic carbon and total nitrogen) and carbon stable isotope analyses ($\delta^{13}C_{oc}$) were performed at ISMAR's premises using a Finnigan DeltaPlus mass spectrometer directly coupled with a FISONS NA2000 Element Analyzer via a CONFLO interface for continuous flow measurements. The standard deviation is 0.15‰ based on replicates of laboratory internal standards. The isotopic composition is reported as per mil (‰) deviation with respect to the Vienna Pee Dee Belemnite (VPDB) standard.

Grain-size analysis was performed on the carbonate-free fraction of the sediment, which was sampled every 5 cm taking out 5 g for each sample. The decarbonisation was obtained with three consecutive washes with 10 ml of hydrochloric acid (20%) to remove the biogenic carbonate component, which reflects vertical marine sedimentation. Deflocculation of the samples was done by successive washes followed by centrifugation (2 times for 10 min at 3000–3500 tr/mn) to accelerate particles settling and siphoning of the supernatant. The samples were then freeze-dried for 48 h and mechanically stirred to ensure particle dispersion. After treatment, samples were stored in sample vials. A micro sample splitter was used to quarter the samples until reaching a representative quantity of sediment to get an obscuration between 8 and 15% during the analysis. The aliquots (around 100 mg) were mixed with water and stirred for four minutes at 15 Hz and went through ultrasonic bath at 80 Hz until complete disaggregation. Despite repeated sets of ultrasonic bath, some samples still contained larger particles identified as pyrite encrustations. The grain-size distribution was obtained with a Malvern Master Sizer 3000 (0.1–2000 μm) at Ifremer's laboratories with the following settings: particle type opaque (Fraunhofer approximation) and non-spherical. The instrument calculated the percentage of grain size for each group (bin) with 21 bins spanning the sortable-silt fraction (SS, 10–63 μm). For statistical redundancy, each sample was measured three times and the average used as the representative result.

3.3. Data handling

3.3.1. Paleo-flow speed reconstruction by sortable silt

The history of a flow speed can be reconstructed through the quantification and characterization of the sortable silt (e.g. McCave et al., 1995; Toucanne et al., 2012; Voigt et al., 2016; Lebreiro et al., 2018). We calculated the mean size of the sortable silt ($\overline{SS}$) and abundance of sortable silt (SS%) according to formulas provided in McCave and Andrews (2019) to estimate changes in flow speed. With this method, the accuracy of the paleo-velocity calculation can be assessed by the correlation coefficient (r) measuring the linear relationship between $\overline{SS}$ for all samples and their abundance percentage in sortable silt (SS%). The closer (r) is to 1 more confidently sediment can be interpreted as

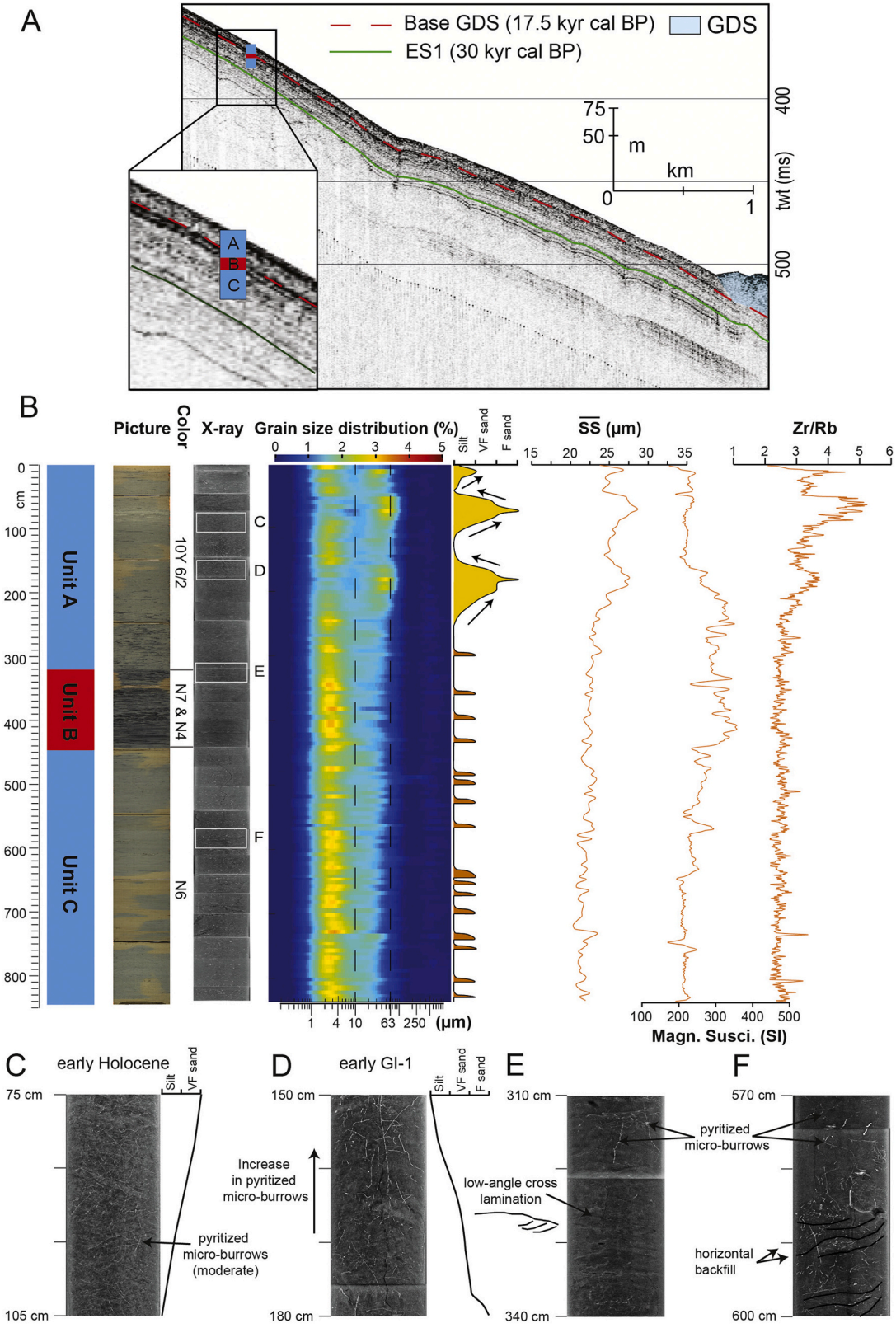

Fig. 3. A) Location of core MS75 in sub-bottom seismic reflection profile. Blue = low seismic amplitude (Units A and C), red = high seismic amplitude (Unit B). The Erosional Surface (ES1) is radiocarbon dated between the Last Glacial Maximum (LGM) and ~ 30 kyr cal BP (Kuhlmann et al., 2015) and seismo-stratigraphically correlated in the study area. B) From left to right: seismic units, core photo and colour scale, X-ray core scan, grain-size distribution and log, $\overline{SS}$, magnetic susceptibility, Zr/Rb ratio. Zoom of X-ray photos: C) non-parallel lamination and moderate abundance of pyritized micro-burrows. D) Non-parallel lamination and increase in pyritized micro-burrows along with decrease in grain size. E) Non-parallel wavy curved lamination, bioturbation and pyritized micro-burrows. F) Pyritized micro-burrows and back-fill. (For interpretation of the references to colour in this figure legend, the reader is referred to the web version of this article.)

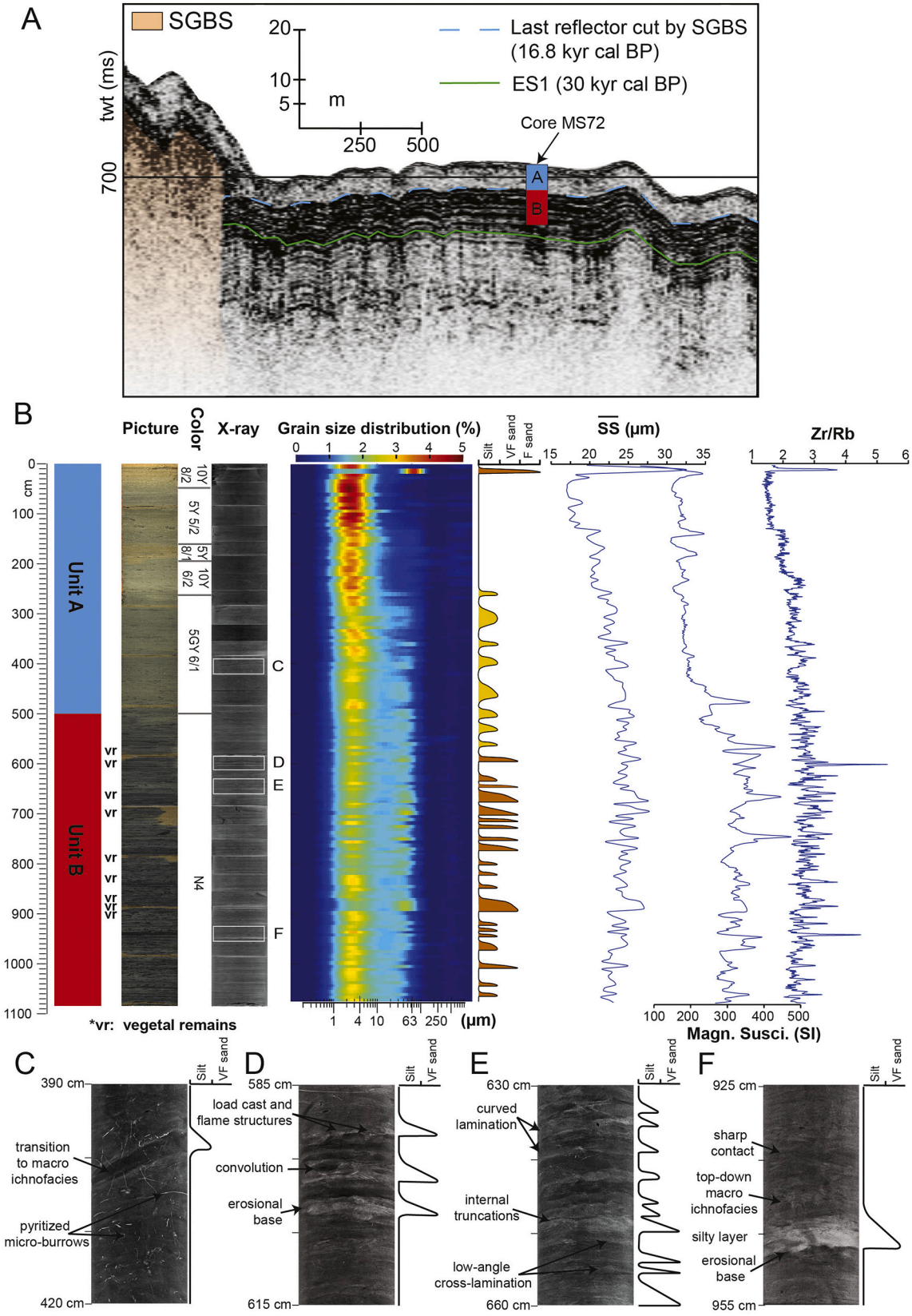

Fig. 4. A) Location of core MS72 in the sub-bottom seismic reflection profile. Blue = low seismic amplitude (Unit A), red = high seismic amplitude (Unit B). B) From left to right: seismic units, core photo and colour scale, X-ray core scan, grain-size distribution and log, $\overline{SS}$, magnetic susceptibility, Zr/Rb ratio. Zoom of X-ray photos: C) change from moderate/high bioturbation by shallow tier structures (pyritized micro-burrows) to macro ichnofacies. D) Intercalations of wavy laminations with low-angle cross-bedding laminations. E) Convolute laminations, load casting and flame structures. F) Lenticular beds characterized by erosional base and sharp contact at the top, close alternation of centimetric silty and muddy layers inside and escaping bioturbating macro fauna. (For interpretation of the references to colour in this figure legend, the reader is referred to the web version of this article.)

Table 1
AMS ^{14}C and calibrated ages based on monospecific and mixed foraminifera. Results are expressed as 2-sigma range.

Core depth (cm)	Age (yr B. P.)	Calibrated age (yr. B.P.) 2σ	Material
Core MS75			
20–21	9220 ± 35	9697–10,134	*Globigerinoides ruber* + *Globorotalia inflata*
71–72	12,600 ± 50	13,823–14,184	*Globigerinoides ruber*
96–97	13,550 ± 95	15,299–16,001	*Globigerinoides ruber* + *Neogloboquadrina incompta*
146–147	14,200 ± 95	16,245–16,951	mixed benthic forams
207–208	14,700 ± 110	16,949–17,655	*Cibicidoides pachyderma*
297.5–298.5	14,850 ± 120	17,138–17,873	mixed benthic forams
457–458	15,150 ± 70	17,614–18,081	*Globigerinoides ruber*
717–718	17,700 ± 100	20,479–21,095	*Globigerinoides ruber*
841.5–842.5	15,800 ± 80	18,369–18,788	*Globigerinoides ruber* + *Neogloboquadrina incompta*
Core MS72			
44.3–44.8	5110 ± 20	5281–5536	*Globigerinoides ruber*
134–135	10,450 ± 40	11,219–11,760	*Globigerinoides ruber*
174–175	11,050 ± 45	12,295–12,674	*Neogloboquadrina incompta*
273–274	13,150 ± 55	14,735–15,306	*Neogloboquadrina incompta*
393–394	14,050 ± 100	16,028–16,756	*Globigerina bulloides* + *Neogloboquadrina incompta*
493–494	15,400 ± 120	17,843–18,474	mixed benthic forams
711–712	15,900 ± 120	18,396–18,932	mixed benthic forams
970–971	16,600 ± 85	19,162–19,739	*Neogloboquadrina incompta*
1077–1078	16,250 ± 85	18,799–19,297	*Globigerinoides ruber* + *Neogloboquadrina incompta*

current-sorted and reliable for providing a flow history (McCave et al., 1995; McCave and Hall, 2006). In order to better differentiate along-slope from downslope sedimentary processes, we identified sediments not affected by bottom-current transport using the 9-point correlation method proposed by McCave and Andrews (2019) and excluded these samples to constrain the bottom-velocity calculations. The method uses the Correl function in Microsoft Excel to evaluate the correlation among nine values of SS% plotted against $\overline{SS}$. The correlation calculated for each sample is then combined with its mean value of the slope based on the same nine values to determine the correlation coefficients for each sample (see McCave and Andrews, 2019). Finally, we estimated the magnitude of absolute changes in flow speed by multiplying the difference between minimum and maximum downcore values in $\overline{SS}$ with the sensitivity of the Malvern laser (1.33 cm s^{-1}/μm; McCave et al., 2017).

3.3.2. Paleo-oceanographic reconstruction by sediment elemental ratios

Marine sediments record paleo-environmental changes over time through variations in major and trace element concentrations (Martinez-Ruiz et al., 2015). In particular, in this study, we used the following elemental ratio proxies:

- Zr/Rb as a grain-size proxy, because Zr is mainly hosted in heavy minerals of coarse-grained siliciclastic sediments and Rb in fine-grained siliciclastic sedimentary rocks (Rothwell and Croudace, 2015). In a few works, Zr/Al has been used as indicative of bottom current strength in relation to the winnowing and enrichment in heavy minerals (e.g. Bahr et al., 2014). However, we decided to use heavy elements for trend reliability.
- Ti/Ca as terrigenous flux proxy, where Ti reflects siliciclastic sediment primarily delivered to the ocean by fluvial transport processes, while Ca reflects changes in the production of calcium carbonate ($CaCO_3$) by marine plankton (e.g., Piva et al., 2008; Govin et al., 2012). The magnetic susceptibility also can be used to broadly infer the prevalence of marine sedimentation or terrigenous input (Vigliotti et al., 2008).
- Ba/Ti as a paleo-productivity proxy, where the biogenic barium is related to the abundance of organic matter (Jaccard et al., 2010).
- S/Cl and pyrite encrustations as evidence of sub-oxic or anoxic conditions, when high concentrations in sulphur lead to sulphate reduction, formation of authigenic iron sulphate and pyrite (e.g. Revel et al., 2015).

3.3.3. Paleo-current and gravity flows identification by sedimentary facies

In addition to the elemental ratios, we used other proxies specifically to distinguish between downslope and along-slope sediment transport: the presence of reworked (e.g. planktonic taxa which are not supposed to be present in that time interval), mixed and broken shells of foraminifera to infer the occurrence of gravity flows and downslope transport. The presence of benthic samples typical of inner-shelf environment (displaced taxa) potentially coeval with other taxa and transported to a deeper environment. Foraminifera assemblages with homogeneous test size were used as proxies of bottom-current sorting.

We searched for sedimentary traction structures in the X-ray images, including horizontal and curved laminae and low-angle cross-laminae, sharp bottom contact (Martín-Chivelet et al., 2008), inverse to normal grading (Stow and Smillie, 2020), as indication of bottom-current fine-grained reworked sediment. We looked into fine-scale sedimentary structures to highlight cross-lamination in normal grading bedding, the presences of loads, flame structures and erosional contacts, lenticular and discontinuous lamination, convolute lamination, water-escape structures, indicative of very rapid deposition under sediment-gravity flows (e.g. Stow and Smillie, 2020).

We used the isotopic fingerprint of plant debris to infer the sediment source area (Tesi et al., 2007; Pedrosa-Pàmies et al., 2015).

Finally, we used ichnofacies of bioturbating fauna to distinguish between: high oxygen levels and intermediate ventilation associated with macro ichnofacies; low oxygen levels and strong bottom currents (Stow and Smillie, 2020) with micro ichnofacies and pyritised microburrows (Petrovic et al., 2019). We used the ichnofacies also to broadly infer the distance from the bottom-current core, based on the assumption that sedimentation rates and ecologically stressful conditions are higher in proximal areas where shallow tier tracemakers (micro ichnofacies) are more abundant, while distal settings favour the development of middle and deep tier tracemakers (macro ichnofacies) (Dorador et al., 2019).

4. Results

4.1. Seismic and sedimentary facies

4.1.1. Core MS75

Distinct seismic facies in sub-bottom seismic reflection profile correspond to the stratigraphic intervals penetrated by core MS75 and allow the identification of three seismic units (Fig. 3A). Unit A (0–320 cm) is characterized by low amplitude and discontinuous reflections and overall transparent seismic facies; unit B (320–450 cm) displays very high amplitude reflections (in red; Fig. 3A); unit C (450–842.5 cm) is characterized by low amplitude almost continuous and parallel reflections.

The seismic units correspond to changes in sediment colour at core scale: pale olive (10Y 6/2) in unit A, medium dark grey (N7) in unit B and medium light grey (N6) in unit C. The X-ray images show wavy to

curved laminations in unit A associated with pyritized micro-burrows (Fig. 3C) that are particularly abundant in the 100–300 cm interval (Fig. 3D). Unit B is characterized by few non-parallel, cross-laminations, whereas pyritized micro-burrows are present only in the uppermost part (Fig. 3E). Unit C shows non-parallel laminations at the top, abundance of pyritized micro-burrows indicating micro-ichnofacies and some horizontal backfill suggesting the presence of transitional ichnofacies (sensu Petrovic et al., 2019) in the bottom part (Fig. 3F) (Table 2).

4.1.2. Core MS72

Two seismic facies characterize the corresponding penetration depth of core MS72 in the sub-bottom seismic reflection profile with a sharp change between low amplitude and discontinuous reflections in unit A (0–500 cm) to high amplitude, continuous and parallel reflections in unit B (500–1078.5 cm) (Fig. 4A).

The striking change in seismic facies corresponds to different sediment colours at core scale: greenish grey in unit A and medium/dark grey in unit B (Fig. 4B). The X-ray images show overall homogenous beds in unit A (Fig. 4B). Abundant macro ichnofacies is present in the upper unit A down to about 250 cm, where is substituted by pyritized micro-burrows (Fig. 4C). Unit B is overall characterized by wavy to curved laminations and moderate macro ichnofacies bioturbation where lamination is less pronounced. Beds characterized by erosional base and convolute lamination, load casting and flame structures are also visible in unit B (Fig. 4D). Closely spaced alternations of laminae broadly curved to wavy at the base and planar upward, showing internal truncations in overall fining-upward beds are present at 600–800 cm (Fig. 4E). Mostly discontinuous, lenticular beds characterize the lower part of unit B, they have an erosional contact, are overlain by rapid alternation of centimetric silty and muddy layers and are topped by a sharp contact. Some burrows truncate the silt layer and the erosional contact at the base (Fig. 4F) (Table 2).

4.2. Grain size distribution

4.2.1. Core MS75

The average grain-size distribution of core MS75 is 70% silt, 24% clay and 6% sand. A slightly higher concentration in sand (8.5%) reflects the bimodal distribution observed in unit A, compared to the unimodal distribution of units B and C (Fig. 3B). In unit A, the bimodal distribution is better defined at 50–90 cm and 150–200 cm with an increase in sand concentration of 13.5% and 10%, respectively (Fig. 3B). Unit A is characterized by $\overline{SS}$ as high as 27 μm, while units B and C have values at least 3 μm lower (Fig. 3B). The grain-size log shows two large inverse to normal grading beds in unit A and normal grading beds characterized by sharp erosional contacts at their base in units B and C. Zr/Rb ratio is overall higher in unit A with peak intervals that are consistent with $\overline{SS}$ trend (Fig. 3B). The magnetic susceptibility shows an opposite trend compared to the previous proxies, with low values where Zr/Rb and $\overline{SS}$ are higher in unit A (Fig. 3B).

4.2.2. Core MS72

The average grain-size distribution of core MS72 is 68% silt, 26% clay and 6% sand. Clay and silt concentrations vary significantly between units A (30% clay, 65% silt) and B (23% clay, 71% silt) (Fig. 4B). The differences in grain-size concentration reflect the unimodal distribution of unit A and the bimodal distribution of unit B (Fig. 4B). Unit A is characterized by $\overline{SS}$ in the range 17–21.4 μm, while unit B shows values 24–27 μm. The grain-size log shows inverse to normal grading beds in the lower unit A and normal grading beds characterized by sharp erosional contacts intercalated with inverse to normal grading beds within unit B. The magnetic susceptibility and Zr/Rb ratios reflect the change in trend between units A and B (Fig. 4B), with overall higher values and variability in unit B compared to unit A (Fig. 4B).

4.3. Paleo-flow reconstruction

The slope and correlation coefficients calculated for core MS75 (Fig. 5A) and core MS72 (Fig. 5B) indicate acceptable values for paleo-flow reconstruction, especially for MS72. However, several sediment layers that are not related to bottom-current transport are present in both cores. Thus, layers with correlation values <0.5 and slope values <0.07 were considered unreliable for paleo-flow reconstruction and rejected, according to the method proposed by McCave and Andrews (2019). The exclusion of the unreliable data led to an increase of the correlation coefficient (r) from 0.744 to 0.876 (red circles in Figs. 5C, D) in core MS75, from 0.839 to 0.877 in core MS72 (blue circles in Figs. 5C, D). Therefore, the reliability tests indicate that core MS75 shows optimal values for paleo-flow reconstruction in unit A, while most of units B and C are unreliable for paleo-flow reconstruction (blue bars in Fig. 5E). On the other hand, core MS72 is overall characterized by hydraulically-sorted sediments, though few unreliable intervals for paleo-flow reconstruction are present in both units A and B (blue bars in Fig. 5E) (Table 2).

4.4. Oxygen and Carbon stable isotopes

The $\delta^{13}C_{oc}$ of plant debris collected in unit B of core MS72 are comprised between 16 and 24 per mil and their C/N molar ratios between 40 and 100 (Fig. 6). The $\delta^{13}C_{forams}$ curve of the planktonic taxon *G. bulloides* (core MS72) shows the lower part, more or less corresponding to the lower sub-interval of the $\delta^{18}O$ curve of the same species, with frequent oscillations of 0.5 per mil amplitude on average, while the middle part (up to ca. 300 cm) has a steadier trend (Fig. 7). The upper interval displays a general decrease of the values punctuated, between 180 and 130 cm, by a temporary increase of the values. The values increase again starting from ca. 50 cm upward (Fig. 7).

The $\delta^{18}O$ curve of the planktonic taxon *G. bulloides* displays, for both cores, a similar trend, which can be divided in three main sub-intervals (Fig. 7). The lower one, from the core bottom up to 680 cm in core MS72 and up to 420 cm in core MS75, shows the heaviest values within an oscillatory trend around +3.5–3.6 per mil. From the top of this interval,

Table 2
Summary of the seismic and sedimentary proxies of cores MS72 and MS75.

Core	Seismic unit, amplitude	Downcore depth (cm)	Sediment grain size and sorting	Sediment structures	Bioturbating fauna ichnofacies	Distance from bottom-current core
MS75	A, Low	0–320	Increase in silt, bimodal, current-sorted	Wavy to curved lamination	Micro	Proximal
	B, High	320–450	Clay, unimodal, unsorted	Low-angle cross lamination	Micro	Decreasingly distal upward
	C, Low	450–842.5		Non-parallel lamination	Micro and transitional	
MS72	A, Low	0–250	Clay, unimodal, current-sorted	Parallel lamination	Macro	Increasingly distal upward
		250–500			Micro	
	B, High	500–1078.5	Increase in silt, bimodal, current-sorted	Wavy, cross and non-parallel lamination, flames and load structures	Macro and micro	Proximal

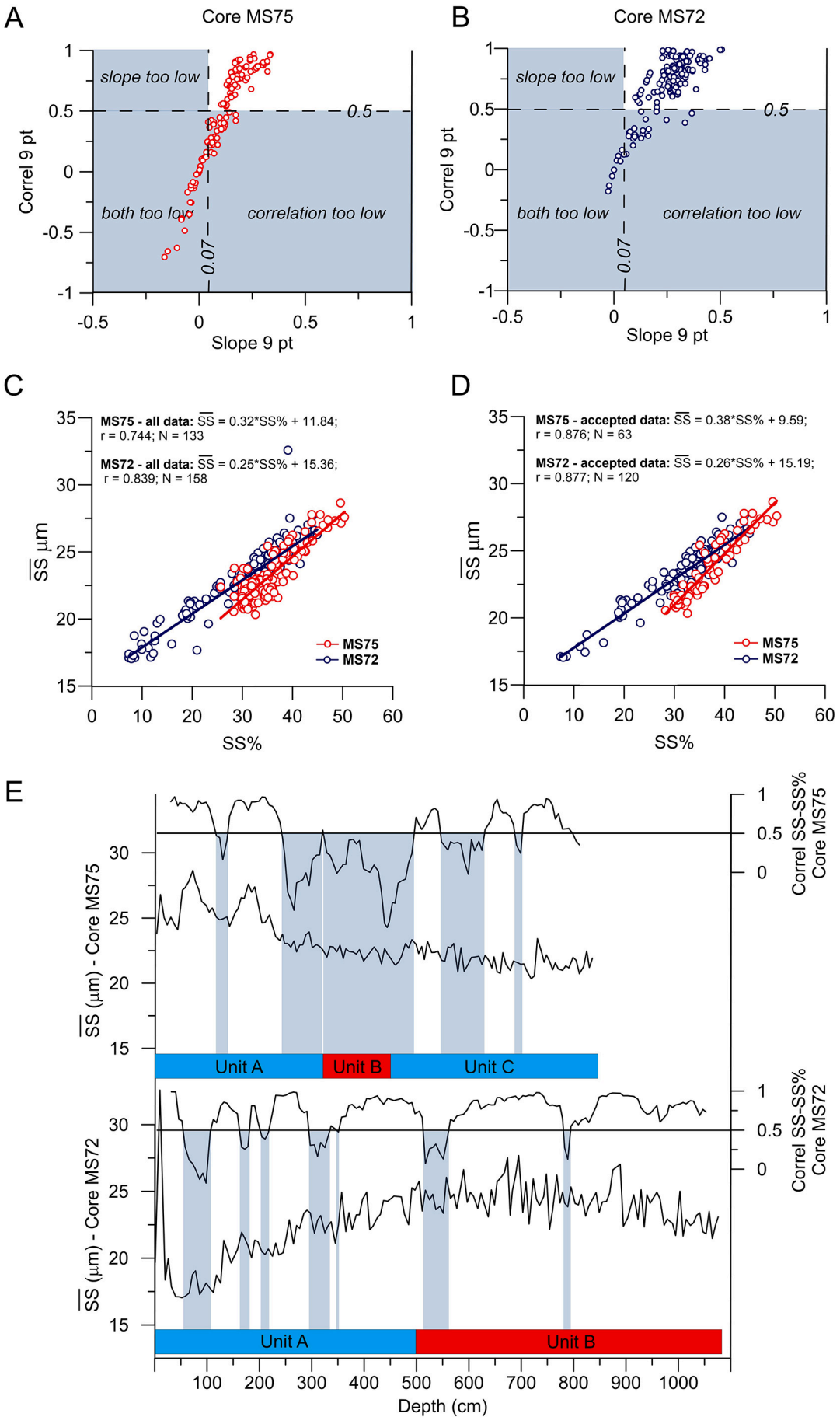

(caption on next page)

Fig. 5. Reliability tests of the downcore correlation coefficients on the 9-points window adapted from McCave and Andrews (2019). Plots of correlation vs slope identify the unreliable $\overline{SS}$ data for cores: A) MS75 and B) MS72 when correlation is <0.5 and slope < 0.07. Plots of SS% vs $\overline{SS}$ to calculate: C) the initial correlation coefficient using all $\overline{SS}$ data and D) the final correlation coefficient after rejection of unreliable data with their linear regressions. E) Pale blue bars indicate sediment layers where paleo bottom-currents are not the main active sediment-transport mechanism. (For interpretation of the references to colour in this figure legend, the reader is referred to the web version of this article.)

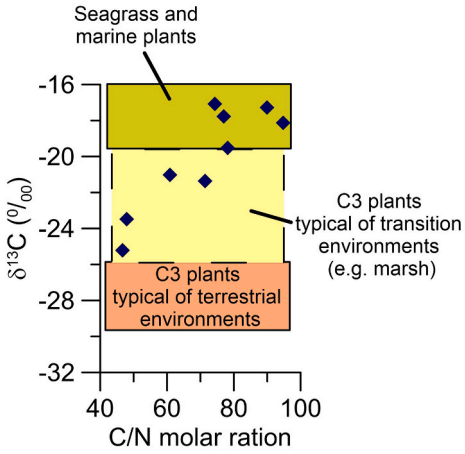

Fig. 6. Bulk composition (carbon/nitrogen ratio combined with stable carbon isotopes) of plant debris sampled in core MS72 (see Figs. 4B and 7 for location of the samples, "vr"). End-members $\delta^{13}C$ values are from Vizzini et al. (2003) and DeLaune and Lindau (1987).

the two curves are characterized by a general decreasing trend culminating at 130 cm in core MS72 and at 13 cm in core MS75 with values between +2.2 and 2.5 per mil. The upper interval shows a further abrupt decrease of the values (< 1.0 per mil). The $\delta^{18}O$ curve of the benthonic foraminifer *B. marginata*, although represented by a quite minor number of measures because the taxon was lacking in several samples, mimics the general trend described for *G. bulloides*, but with absolute values higher than *G. bulloides* (Fig. 11).

4.5. Foraminifera assemblages and ecozones

The turnovers observed in the foraminifera assemblages in the two cores allowed recognizing planktonic (Pl 1–4) and benthonic (Be 1–4) ecozones (Table 3). However, several samples (green "r" in Fig. 7) included rare specimens of benthonic epiphytic taxa (*Asterigerinata mamilla*, *Elphidium crispum*, *Reussella spinulosa*) or belonging to species typical of inner-middle shelf environment (*Ammonia beccarii*, *Elphidium decipiens*, *Elphidium advenum*, *Elphidium poyeanum*). Other samples were well-sorted and displayed the whole foraminifera assemblage characterized by a quite homogeneous test size (grey "r" in Fig. 7) or by the presence of very rare larger specimens (black "r" in Fig. 7).

4.6. Age-depth model

The chronology of the two cores integrates the results and calibration of radiocarbon dating (Table 1), eco-biostratigraphy (Table 3), oxygen and carbon stratigraphy and allows determining an age-depth model (Table 4).

The planktonic foraminiferal ecozones can be compared with similar ecozones described for this area (Vergnaud-Grazzini et al., 1988; Sprovieri et al., 2003; Minisini et al., 2007; Rouis-Zargouni et al., 2010; Ferraro et al., 2018) and in other Mediterranean basins (Asioli et al., 1999; Perez-Folgado et al., 2003; Melki et al., 1999; Lirer et al., 2013; Siani et al., 2010). The paleoenvironmental interpretation of these ecozones provided a sequence of events correlatable with Mediterranean and extra-Mediterranean paleoclimate events during the Late Quaternary (event stratigraphy) (Asioli et al., 2001; Sprovieri et al., 2003). Moreover, the turnovers observed in the planktonic foraminifera assemblages allowed recognizing the following (temporary) disappearances and/or (re)occurrences of taxa, already reported in the literature.

- Peak of *Globorotalia truncatulinoides* right coiling during the late Holocene. This event was reported in the Strait of Sicily also by Sprovieri et al. (2003), dated at 4300 yr cal. BP (4280 ± 40 ^{14}C age) by Minisini et al. (2007), at 2500 yr BP by interpolation by Rouis-Zargouni et al. (2010) and Desprat et al. (2013), and at 3600 yr BP (4139 ± 37 ^{14}C age) by Ferraro et al. (2018). The discrepancy between the calibrated ages by Minisini et al. (2007) and Ferraro et al. (2018) depends on the applied reservoir age (ΔR value of 71 ± 50 yr by Minisini et al., 2007 and no ΔR correction by Ferraro et al., 2018), as the radiocarbon ages are very close. Here we preferred the calibrated age by Minisini et al. (2007), as based on the reservoir correction available for Strait of Sicily in the Calib dataset, while we rejected the much younger age by Rouis-Zargouni et al. (2010) confirming the age uncertainties for the upper 80 cm of core MD04-2797CQ suggested by Desprat et al. (2013).
- Temporary disappearance of *G. truncatulinoides* (along with a *Globorotalia inflata* frequency minimum) corresponding to the base of Sapropel 1 equivalent (Sprovieri et al., 2003; Minisini et al., 2007). We ascribed the age 10,000 yr cal. BP to this bioevent which detects the base of the S1a interval by Minisini et al. (2007), dated at 9340 ± 120 ^{14}C age (10,052 yr cal. BP median probability). This age is in full agreement with the onset of the Sapropel 1 deposition in the Eastern Mediterranean and Adriatic Sea (Tesi et al., 2017).
- First abrupt increase of *Globigerinoides ruber* and warm species and concurrent last occurrence of *Globorotalia scitula*, marking the beginning of Greenland Interstadial 1 (GI-1)/Bølling-Allerød (Vergnaud-Grazzini et al., 1988; Perez-Folgado et al., 2003; Sprovieri et al., 2003; Minisini et al., 2007; Rouis-Zargouni et al., 2010).

The $\delta^{18}O$ *G. bulloides* curve of the two cores have been correlated with other similar Mediterranean records in the Alborán Sea (core MD95–2043 from Cacho et al., 1999), the Western Mediterranean (Menorca drift, core MD99–2343 from Sierro et al., 2005) and the Strait of Sicily (core MD04-2797CQ from Rouis-Zargouni et al., 2010). The second step of the Termination I (T IB) with its characteristic abrupt decrease of the $\delta^{18}O$ values, as well as the preceding GS-1 interval, can be detected quite easily in both the studied cores (blue area in Fig. 7). The first step of the Termination I (T IA), which includes the Heinrich Stadial 1 episode (HS 1) (Heinrich, 1988; Bond et al., 1992; Hodell et al., 2017) is also visible, although the progressive decreasing $\delta^{18}O$ values culminating in the low peak of $\delta^{18}O$ at the Heinrich Event 1 (ca. 16 ka, dashed blue line in Fig. 7) is at least 300 cm thick in both cores. The correlation of the HS1 interval is further constrained by the stratigraphic position of the foraminifera bioevents: first increase of *G. ruber* at the base of GI-1; Last Occurrence (LO) of *G. scitula* just before GI-1; the continuous presence of *G. ruber* between 23 and 18 kyr BP, as also reported by Perez-Folgado et al. (2003) in the Alborán Sea and in the Strait of Sicily by Rouis-Zargouni et al. (2010).

In addition to the oxygen isotope stratigraphy of *G. bulloides*, we also used the $\delta^{13}C$ *G. bulloides* record in core MS72 to strengthen the chronology. Indeed, it has been demonstrated that across the Mediterranean the $\delta^{13}C$ *G. bulloides* record displays a consistent pattern during the last glacial/post glacial interval with two negative excursions during T IA and IB intercalated by intervals of heavier values during the Younger Dryas (GS-1) and the present time (Vergnaud-Grazzini et al., 1986,

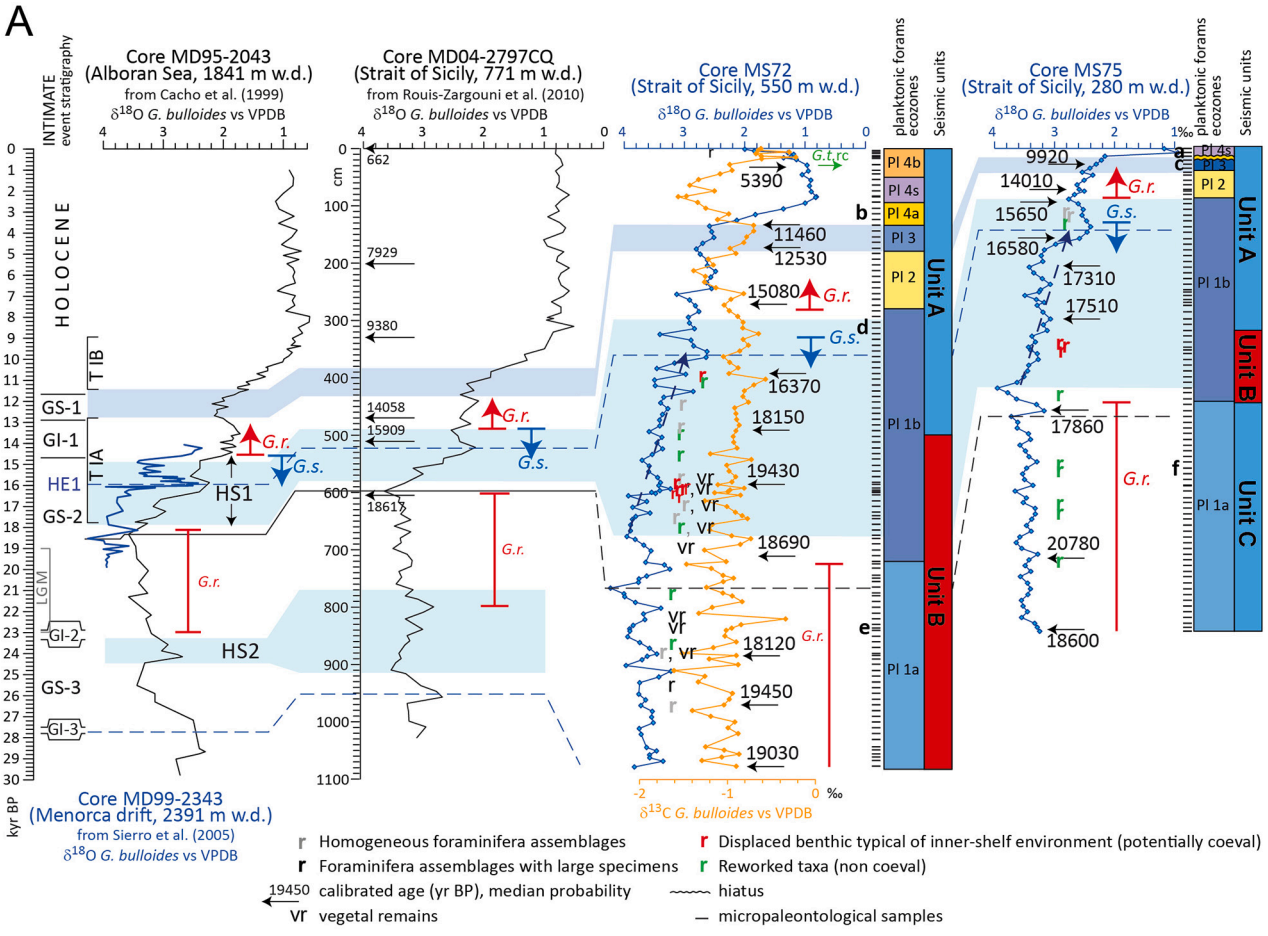

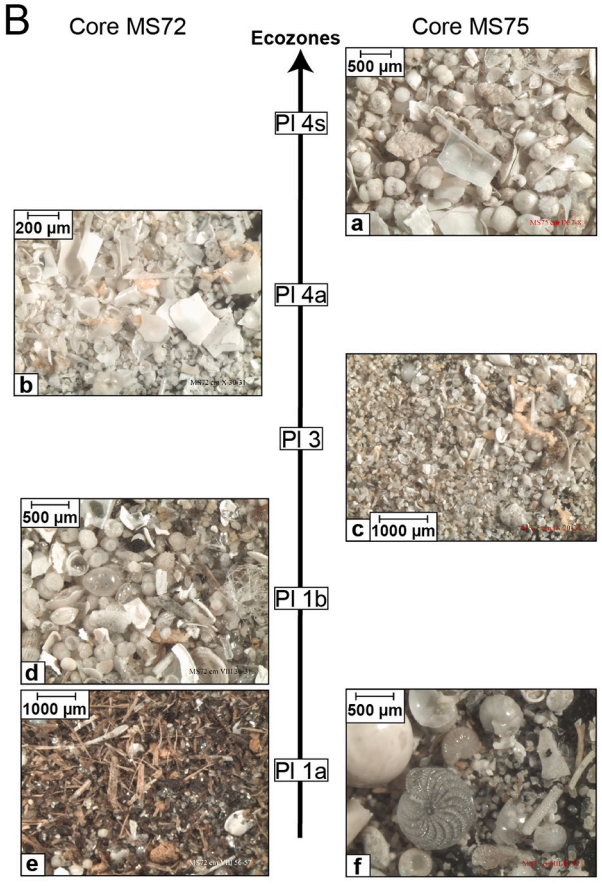

(caption on next page)

Fig. 7. A) Stratigraphic correlation of the $\delta^{18}O$ record of cores MS72 and MS75 compared with the reference cores from the Alborán Sea, Menorca Drift and Strait of Sicily (see references on top of each core). The stratigraphic position of the main foraminiferal bioevents is reported. The reference INTIMATE event stratigraphy is from Björck et al. (1998) and Blockley et al. (2012). The ages reported for the reference core MD04-2797CQ are calibrated (yr BP) according to Rouis-Zargouni et al. (2010). The data were not corrected for the ice volume effect. G.r. = *Globigerinoides ruber*, G.s. = *Globorotalia scitula*, G. tr. rc = *Globorotalia truncatulinoides* right coiling, GS = Greenland Stadial, GI = Greenland interstadial, HS = Heinrich Stadial, LGM = Last Glacial Maximum chronozone according to Mix et al. (2001). B) Micrographs of foraminifera assemblages and their ecozones: a & b) hemipelagic sample without terrigeneous; c) foraminifera with terrigenous; d) cold-water planktonic foraminifera showing different test sizes (no hydraulic selection); e) abundant vegetal debris with fine terrigenous; f) foraminifera assemblage, including taxa typical of inner shelf (*Elphidium crispum*), with fine terrigenous.

1988; Ariztegui et al., 2000). This pattern is visible in core MS72.

Radiocarbon datings help refining the age model, although some of them provide ages slightly older than expected based on the oxygen-isotope stratigraphy, mainly below the relative peak of $\delta^{18}O$ of the Heinrich Event 1 at ca. 16 kyr BP, and a few age reversals also occur. The frequent presence of displaced, reworked or sorted foraminifera suggests transport processes possibly shedding sediment of ages not much older than the in situ sediments.

At the top of core MS72 $\delta^{18}O$ and $\delta^{13}C$ *G. bulloides* records show an anomalous trend: $\delta^{18}O$ curve has values too high (up to 2 per mil) and $\delta^{13}C$ show oscillations too wide. The concurrent presence of reworked foraminifera confirms that the upper part of core MS72 (12 cm) is disturbed. Similarly, the uppermost part of core MS75 shows some inconsistency among ^{14}C age (9920 yr cal. BP, corresponding to the beginning of the deposition of Sapropel 1 in the Levantine Basin), $\delta^{18}O$ values (2.2 per mil, values relatively high and more coherent with the beginning of the Holocene rather than the base of Sapropel 1 deposition) and planktonic ecozone (more relatable with the pre-Boreal than with the GS-1, because of the common presence of *G. ruber*). Therefore, considering the lack of $\delta^{18}O$ values typical of the abrupt shift of T IB (recorded in core MS72), sediment erosion is likely present between 7 and 20 cm. Overall, the mean temporal resolution over the deglacial interval is ca. 11–14 yr/cm.

4.7. Sedimentation rates and age of emplacement of MTDs

Based on the reconstructed age-depth model, a linear sedimentation rate (LSR) was calculated for both cores. LSR was obtained from a linear interpolation between the intercepts of the control points that have not been rejected (Table 4). In core MS75, sedimentation rates range from 17 to 114 cm/kyr and briefly peak at 1322 cm/kyr in the early phase of HS1 and 770 cm/kyr in the last phase of LGM (Fig. 8A). In core MS72, sedimentation rates range from 11 to 95 cm/kyr and peak at 230 cm/kyr in the early phase of HS1 and 370 cm/kyr in the last phase of LGM (Fig. 8B).

The age-depth model allowed to constrain the age of significant reflections in the sub-bottom profiles and tentatively dating the age of emplacement of two submarine landslides identified by their chaotic seismic facies: the Gela Drift Slide (GDS in Fig. 3A) and the South Gela Basin Slide (SGBS in Fig. 4A). For GDS, the high amplitude reflection at the base of the slide accumulation correlates with the top of unit B of core MS75 and, according to the age model, corresponds to 17.5 kyr cal. BP (red dashed line, Fig. 3A). Therefore, GDS must have been emplaced after ca. 17.5 ka. For SGBS, the last seismic reflection cut by the slide correlates with the top of unit B of core MS72, which dates at 16.8 kyr cal. BP (blue dashed line in Fig. 4A) suggesting that SGBS must be younger.

4.8. Paleoenvironmental elemental proxies

Based on the reconstructed chronology, the elemental ratio proxies inform on periods of increased/decreased sea-bottom oxygenation, biogenic activity and productivity.

4.8.1. Core MS75

From 18.6 to 18 kyr BP S/Cl ratio shows low values around 0.01, increasing to 0.05 around 18 kyr BP and varying around 0.03 until 8 kyr BP (Fig. 9).

From 18.5 to 17 kyr BP Ti/Ca ratio shows values >0.04, decreasing to 0.03–0.04 until 15 kyr BP where a drastic decrease occurs with values nearing 0.01. At 13 kyr BP Ti/Ca increases above 0.02 before decreasing again down to 0.01 around 12.7 ka (Fig. 9).

4.8.2. Core MS72

Ba/Ti, is higher (−0.02) from 19 until 12.8 kyr BP along with higher values in S/Cl and stronger variations up to 0.17 from 19 to 15.8 kyr BP (Fig. 10). From 15.08 to 12.8 kyr BP, Ba/Ti stays high while fewer variations are observed in S/Cl. At 12.8 kyr BP, Ba/Ti values drastically decrease (−0.09) at the end of GI-1 and S/Cl shows constant values close to zero. From 11.5 to 4 kyr BP Ba/Ti stays low as well as S/Cl.

Since 19 ka Ti/Ca shows high values around 0.05 until 15.08 kyr BP when a drastic decrease down to 0.02 occurs (Fig. 10). Towards the end of GI-1, Ti/Ca ratio increases until reaching values up to 0.03 around 12 ka (GS-1) and keep similar values during the Holocene.

5. Discussion

5.1. Deciphering along-slope and downslope processes in sedimentary records

Two sediment cores from the upper and lower slope of Gela Basin, Strait of Sicily, were collected along a sediment drift deposited under the activity of the Levantine Intermediate Water (LIW) and provided an unprecedented stratigraphically-expanded sedimentary record spanning the last phase of LGM and early phase of HS1 (~ 19–16 kyr BP) for the Central Mediterranean Sea. In particular, the interval 19–18 kyr BP is characterized by exceptionally high linear sedimentation rates in both cores (LSR, Fig. 8). Various proxies allow identifying the sedimentary processes that concur to obtain such deposition.

During 19–16 ka, sediment core MS75 records weak bottom-current velocities (Fig. 12) and prevailing deposition of clay in unimodal grain size distribution (Fig. 3B, Table 2) which exclude the presence of a persistent contour-current regime along the upper slope. The presence of sparse laminations and normal grading beds (Fig. 3B) together with reworked foraminifera (Fig. 7) indicate that moderate downslope sediment transport is taking place in the upper slope. Variations in S/Cl and presence of authigenic pyrites and pyritized micro burrows are all indicative of lack of oxygen/ventilation and stressful conditions at the sea bottom (Fig. 9) whereas transitional ichnofacies seems to indicate less stressful condition, that may be related to sediment-gravity flows coarsely-spaced in time.

On the contrary, during 19–16 ka, in sediment core MS72, high $\overline{SS}$ and bimodal grain size distribution (Fig. 4B, Table 2), combined with increased hydraulic sorting of foraminifera (Fig. 7), indicate that strong bottom-currents are actively moving sediments on the lower slope. The seismic facies points to turbidite deposition (Fig. 4A), the grain-size log highlights inverse to normal grading beds typical of contourite deposition intercalated with normal grading beds typical of rapid downslope deposition (Fig. 4B). The sedimentary facies indicate the presence of products of storm waves (tempestites) intercalated with sediment-gravity flows (turbidites) with a combination and overprinting of traction transport and suspended load (Fig. 4D). At the same time, convolute and flame structures seem produced just below the water-sediment interface by a passing current or by downslope sliding on the

Table 3
Foraminifera ecozones and inferred paleoenvironments for cores MS72 and MS75 along with the corresponding time intervals/events to which the ecozones were equated. Bolded and underlined names define the abundant and common species, respectively.

Ecozones	Depth	Assemblage	Environment	References	Time interval
Pl 4b	MS72 = 0–54 cm, not recognized in MS75	***Globigerinoides ruber, Globorotalia inflata***, Globorotalia truncatulinoides (in MS72 r.c. dominates at cm 28–29 in MS72, while l.c. dominates cm 0–28), *Globigerinoides sacculifer*, *Orbulina universa*, *Globigerinella siphonifera*, *Globigerina bulloides*, *Turborotalita quinqueloba*, *Globigerinella calida*, *Globoturborotalita rubescens*	Warm water assemblage with deep dwellers (winter mixing)	Vergnaud-Grazzini et al. (1988), Sprovieri et al. (2003), Minisini et al. (2007), Rouis-Zargouni et al. (2010), Ferraro et al. (2018)	Late Holocene (0-6kyr BP)
Pl 4 s	MS72 = 54–94 cm, MS75 = 0–8 cm	***G. ruber*** (including *G. ruber* pink variety with thin and inflated test), *O. universa*, *G. sacculifer*, *G. siphonifera*, *G. bulloides*, *T. quinqueloba*, *G. rubescens*, *G. inflata*	Warm water assemblage with strong decrease of deep dwellers (weak winter mixing)	Vergnaud-Grazzini et al. (1988), Sprovieri et al. (2003), Minisini et al. (2007), Rouis-Zargouni et al. (2010)	Holocene (Sapropel 1 deposition) (6-10kyr BP)
Pl 4a	MS72 = 94–134 cm, MS75 = 13–14 cm	***G. ruber, G. inflata, G. truncatulinoides,*** *G. glutinata*, *G. bulloides*, *T. quinqueloba*, *Neogloboquadrina incompta*	Temperate water assemblage with deep dwellers (winter mixing)	as above	Early Holocene (pre-Boreal) (10–11.5kyr BP)
Pl 3	MS72 = 134–180 cm, MS75 = 20–41 cm	***G. bulloides, N. incompta, T. quinqueloba,*** *G. glutinata*, *G. inflata*, *G. ruber* RR/absent	Cold and productive water assemblage	as above	Late Pleistocene (GS-1) (11.5–12.8kyr BP)
Pl 2	MS72 = 180–280 cm, MS75 = 41–88 cm	***G. ruber, G. inflata, T. quinqueloba,*** *G. bulloides*, *N. incompta*, *Orbulina universa*, *G. glutinata*, *Globorotalia truncatulinoides*	Temperate water assemblage, DCM developed, winter mixing	as above	Late Pleistocene (GI-1) (12.8–14.7kyr BP)
P 1b	MS72 = 280–720 cm, MS75 = 88–442 cm	***T. quinqueloba, N. incompta*** **and** ***G. bulloides***, *Globorotalia scitula*, *G. glutinata*	Cold and productive water assemblage	as above	Late Pleistocene (GI-1) (14.5–18 kyr BP)
Pl 1a	MS72 = 720–1079 cm, MS75 = 442–842 cm	***T. quinqueloba, N. incompta, G. bulloides,*** *G. scitula*, *G. glutinata*, *G. ruber* (continuous presence)	cold and productive water assemblage	Sprovieri et al. (2003), Rouis-Zargouni et al. (2010)	Late Pleistocene >18 kyr BP
Be 4	MS72 = 0–54 cm and 94–134 cm, MS75 = 8–14 cm	assemblage not very rich; ***Uvigerina mediterranea,*** *Gyroidinoides altiformis, Hyalinea balthica, Melonis barleeanum, Bulimina marginata, Cibicidoides pachyderma, Cassidulina laevigata carinata, Bigenerina nodosaria, Pseudoclavulina crustata, Bulimina costata, Amphycorinae scalaris, Planulina wuellerstorfi, Lenticulina stellata, Lenticulina peregrina, Gyroidinoides* spp., *Glomospira charoides*, miliolids (*Biloculinella labiata, Sigmoilinita tenuis, Sigmoilopsis schlumbergeri, Quinqueloculina seminulum*)	upper slope (mesotrophic environment)	Jorissen (1987), De Stigter et al. (1998), De Rijk et al. (1999), Schmiedl et al. (2010), Minisini et al. (2007)	Holocene (0–11.7kyr BP) except Sapropel 1 interval
Be 4 s	MS72 = 54–94 cm, MS75 = 0–8 cm	foraminifera scarce or rare; *U. mediterranea*, *G. altiformis*, *M. barleeanum, Uvigerina peregrina*, *Chilostomella mediterranensis*, *Sphaeroidina bulloides*, *C. laevigata carinata, B. nodosaria*, *P. crustata*, *A. scalaris, Lenticulina* spp., miliolids (*Biloculinella globula*, *Pyrgo depressa*, *Triloculina trigonula*, *Spiroloculina* spp., *S. schlumbergeri*)	upper slope (mesotrophic environment, with more organic matter accumulation and lower bottom ventilation)	Jorissen (1999), De Rijk et al. (1999), Minisini et al. (2007)	Holocene (Sapropel 1 deposition) (6–10 kyr BP)
Be 3	MS72 = 134–180 cm, MS75 = 20–41 cm	***U. mediterranea, Brizalina dilatata,*** *C. laevigata carinata*, *G. altiformis*, *H. balthica*, *M. barleeanum*, *B. marginata*, *C. pachyderma*, *Bolivina albatrossi*, *Globobulimina affinis*, *Bulimina inflata*, *B. costata*, *Hanzawaia boueana, S. bulloides*, *Gyroidinoides* spp., *Hoeglundina elegans, G. altiformis, P. crustata, Pyrgo bulloides*, *P. depressa*, *Spiroloculina* spp., *S. tenuis, S. schlumbergeri, Q. seminulum, Triloculina tricarinata*	upper slope	Vergnaud-Grazzini et al. (1988), Minisini et al. (2007)	Late Pleistocene (GS-1) (11.5–12.8kyr BP)
Be 2	MS72 = 180–280 cm, MS75 = 41–88 cm	***C. laevigata carinata, U. mediterranea, U. peregrina, B. dilatata,*** *G. altiformis*, *H. balthica*, *M. barleeanum*, *S. bulloides*, *B. marginata*, *C. pachyderma*, *G. affinis, C. mediterranensis, B. costata, H. boueana, Gyroidinoides* spp., *H. elegans, Planulina ariminensis, P. bulloides, Spiroloculina* spp., *S. tenuis, S. schlumbergeri, Q. seminulum, Quinqueloculina padana, Articulina tubulosa*	upper slope	as above	Late Pleistocene (GI-1) (12.8–14.7 kyr BP)
Be 1b	MS72 = 280–720 cm, MS75 = 88–442 cm	***B. dilatata, Brizalina aenariensis, Brizalina alata,*** *C. laevigata carinata*, *B. albatrossi*, *H. balthica*, *M. barleeanum, S. bulloides, B. inflata, Nonion depressulus, B. nodosaria*, *B. marginata*, *U. peregrina, Trifarina angulosa, G. affinis, C. pachyderma, G. altiformis, Hanzawaia boueana, P. bulloides, P. depressa, Spiroloculina spp, Cycloforina tenuicollis, S. tenuis, S. schlumbergeri, Q. seminulum, Biloculinella* spp., *A. tubulosa* in core MS72 and *Sigmoilina sellii* in core MS75	upper slope (mesotrophic environment, with low bottom ventilation)	as above	Late Pleistocene 14.5–18 kyr BP
Be 1a					

(*continued on next page*)

Table 3 (*continued*)

Ecozones	Depth	Assemblage	Environment	References	Time interval
	MS72 = 720–1079 cm, MS75 = 442–842 cm	rich assemblage; ***B. aenariensis, B. alata,*** *B. dilatata*, *M. barleeanum*, *Valvulineria complanata*, ***C. laevigata carinata*** and ***H. balthica*** and ***B. marginata*** (MS75), *S. bulloides, B. inflata, G. affinis, C. pachyderma, U. peregrina, B. nodosaria, P. bulloides, Spiroloculina* spp., *Miliolinella subrotunda, S. tenuis, S. schlumbergeri, Q. seminulum, Q. padana, A. tubulosa* (MS75),	upper slope (mesotrophic environment, with low bottom ventilation)	Sprovieri et al. (2003), Rouis-Zargouni et al. (2010)	Late Pleistocene >18 kyr BP

Table 4
Age-depth model adopted in this study.

Core depth (cm)	Control point (yr BP)	Source	Note
Core MS75			
10	8000	Ecozone Pl 1 s	
13	11,700	top ecozone Pl 2 (GS-1)	
20.5	9920	^{14}C AMS (median probability)	*rejected*
41	12,900	base ecozone Pl 2 (GS-1)	
71.5	14,010	^{14}C AMS (median probability)	
96.5	15,650	^{14}C AMS (median probability)	
136.5	16,000	δ^{18}O negative peak HS1 core MD99–2343 (Sierro et al., 2005)	
146.5	16,580	^{14}C AMS (median probability)	
207.5	17,310	^{14}C AMS (median probability)	
298	17,510	^{14}C AMS (median probability)	
417	17,600	δ^{18}O positive peak base HS1 core MD99–2343 (Sierro et al., 2005)	
457.5	17,860	^{14}C AMS (median probability)	*rejected*
457.5	18,100	δ^{18}O negative peak below HS1 core MD99–2343 (Sierro et al., 2005)	
717.5	20,780	^{14}C AMS (median probability)	*rejected*
842	18,600	^{14}C AMS (median probability)	
Core MS72			
13.5	4300	peak *G. truncatulinoides* r.c. (Minisini et al., 2007)	
44.5	5390	^{14}C AMS (median probability)	
94	10,000	Base ecozone Pl 1 s	
134.5	11,460	^{14}C AMS (median probability)	
174.5	12,530	^{14}C AMS (median probability)	
273.5	15,080	^{14}C AMS (median probability)	
360	16,000	δ^{18}O negative peak HS1 core MD99–2343 (Sierro et al., 2005)	
393.5	16,370	^{14}C AMS (median probability)	
493.5	18,150	^{14}C AMS (median probability)	*rejected*
587.5	19,430	^{14}C AMS (median probability)	*rejected*
676	17,600	δ^{18}O positive peak base HS1 core MD99–2343 (Sierro et al., 2005)	
711.5	18,690	^{14}C AMS (median probability)	*rejected*
733	18,100	δ^{18}O negative peak below HS1 core MD99–2343 (Sierro et al., 2005)	
885.5	18,120	^{14}C AMS (median probability)	*rejected*
970.5	19,450	^{14}C AMS (median probability)	*rejected*
1077.5	19,030	^{14}C AMS (median probability)	

unconsolidated mud (e.g. Potter et al., 2005). Therefore, the load structures can be a direct sign of the high sedimentation rates recorded in the lower slope during the last phase of LGM and early HS1 (Fig. 4E). Furthermore, the presence of bioturbating fauna, characterized by macro ichnofacies signal, that tend to rework the upper parts of a bed while leaving the lower parts unaffected (Fig. 4F), are indicative of turbidites interbedded with less energetically accumulated contourites (e.g. Stow and Smillie, 2020).

Overall, intermediate characteristics between silty-muddy turbidites and muddy contourites are thus apparent in the lower slope and suggest the activity of contour currents during or shortly after turbidite deposition, as proposed for margins where the interplay between downslope and along-slope processes is more frequent (Fig. 4F; Massé et al., 1998; Fonnesu et al., 2020). The concomitant presence of both displaced (e.g. *Elphidium decipiens)* and hydraullically-sorted foraminifera confirm the overlap of two transport mechanisms. Furthermore, the presence of plant debris from shallow water marine domain (e.g. *Posidonia oceanica*) and transitional domains (e.g. marsh, Fig. 6) strengthen the evidence of sediment input from the inner-mid shelf through the action of persistent gravity flows active until at least 17.5 ka (Figs. 4, 11). The high sedimentation rate associated with downslope sediment transport superimposed by sustained lateral advection caused overall low oxygen conditions, as testified by the presence of sediments rich in iron sulphate and benthic foraminifera resistant to low oxygen stressful conditions induced by rapid burial. Furthermore, shallow tier structures left by bioturbating fauna are indicative that the bottom-current core was located near the lower slope (Table 2).

During sea-level low stands and glacial periods, the shoreline is closer to the shelf edge and sediment input to the slope increases, this has been observed particularly in the last phase of LGM when also several submarine landslides are believed to have been emplaced along the continental margins (e.g. Lee, 2009). High sedimentation rates during glacial periods are thus normal, however strong bottom-currents active along a specific continental margin imply an even larger sediment availability along the slope to counterbalance bottom erosion (Miramontes et al., 2016). Marked increase in sedimentation rates during glacial periods, 2–7 times those in interglacials, are often considered a function of reduction of vegetation cover during arid conditions, resulting in increased erosion and basin sediment flux (e.g. McNeill et al., 2019). Furthermore, frequency and magnitude of hyperpycnal flows are known to increase during arid climate when relative sea level rises in areas with a wide continental shelf (Mulder et al., 2003), as is the case of the Malta Plateau. The sea level was rising with rates of ca. 12 m/kyr between 19 and 17.5 ka (Lambeck et al., 2014) and the scattered plot of Zr/Rb indicating high Zr content could be correlated with flood events carrying greater coarse-grain sediment loads (e.g. Wang et al., 2011). High LSR observed in the northern Gela Basin were explained by the occurrence of intermittent hyperpycnal flows (Kuhlmann et al., 2015). However, in the southern Gela Basin the presence along the slope of epiphytic benthic taxa (Fig. 11) and the source apportionment of the plant debris (Fig. 6) suggest a sediment provenance from the inner and middle shelf. Therefore, all data including terrigenous proxy (Ti/Ca) concur to exclude a direct riverine sediment source and indicate that sediment was sourced from shelf erosion during low stands of sea level and moderate sea-level rise.

The presence of gullies on the northern slope of the Gela Basin (Fig. 1C) may have represented preferential sediment by-pass from shelf to basin, as elsewhere envisaged (Ricketts and Evenchick, 1999), together with along-slope sediment transport from north to south sustained by strong bottom currents concomitantly active at the seafloor in the lower slope. The sediment by-pass may have shut down at 18–17.5 ka, when the two sediment cores face a drastic drop of LSR and bottom-current velocities peak maximum intensity in the lower slope (Figs. 10 and 12). Moreover, the significant change in magnetic susceptibility trend between units A and B of core MS72 (Fig. 4B) may indicate different sources with sediment supply from downslope gravity flows before 17.5 ka and prevailing marine deposition afterwards. The drastic reduction in sedimentation rate can thus be explained by a combination of factors: prevailing erosion over deposition by bottom-current action, reduced along-slope apportion of sediment from the north together with

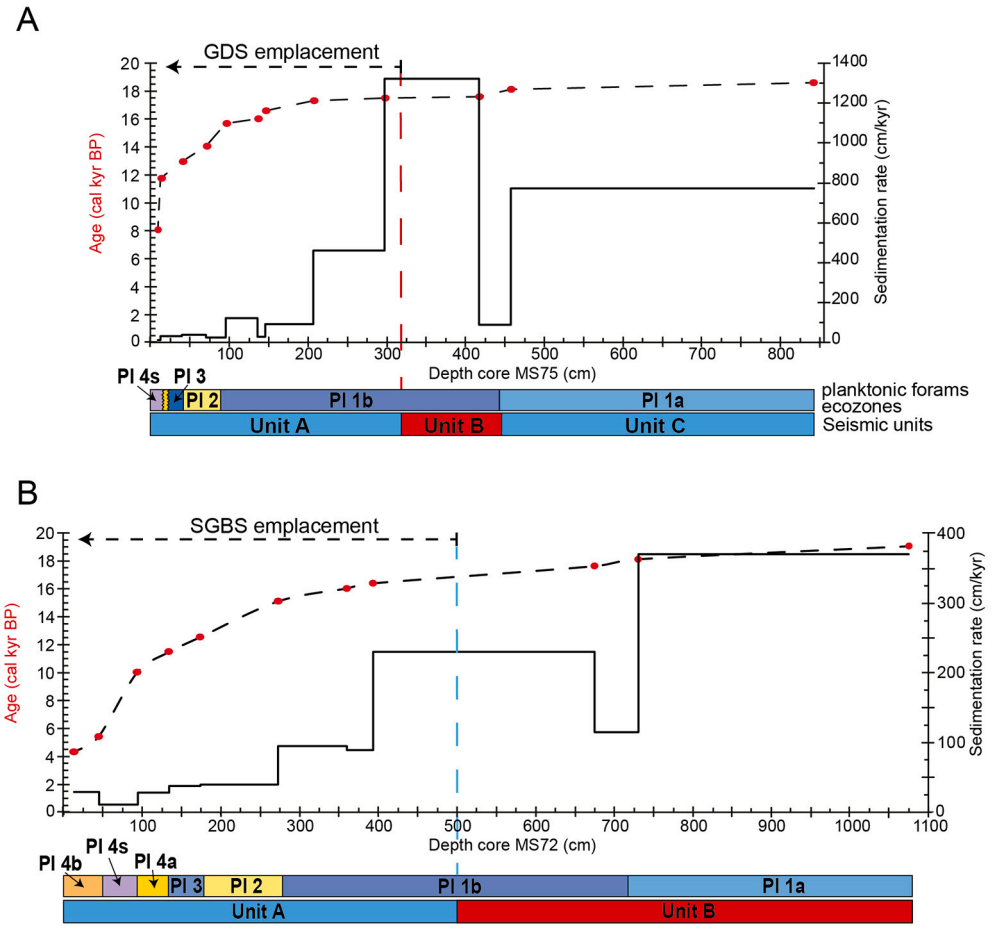

Fig. 8. Linear sedimentation rates (LSR) of cores MS72 (A) and MS75 (B). Red dots indicate the ^{14}C calibrated ages. Planktonic foraminifera ecozones and seismic units are displayed below the age-depth plot. The dashed vertical lines identify the estimated age of emplacement of mass-transport deposits GDS and SGBS. (For interpretation of the references to colour in this figure legend, the reader is referred to the web version of this article.)

reduced sediment input from sediment-gravity flows in the southern slope of the Gela Basin.

5.2. LIW intensity and interface variations in the Gela Basin during deglaciation

By excluding both the stratigraphic intervals deposited under downslope processes (tempestites and turbidites, Fig. 4B) and those with evidence of reworking/displacement/hydraulic selection of foraminifera (yellow stripes in Fig. 11) of core MS72, we are able to reconstruct the post-LGM bottom current dynamics in the Gela Basin and making inferences about the thermohaline Mediterranean circulation.

During the last phase of LGM and early HS1 (19.4–18 kyr cal. BP) $\delta^{13}C_{forams}$ and $\delta^{18}O$ (Fig. 11) and planktonic assemblages are typical of cold and productive waters, benthic assemblages are dominated by species expected in mesotrophic environment with low bottom ventilation (ecozones PI 1a and Be 1a in Table 3, respectively). The $\overline{SS}$ increases by 4–6 μm with an increase in current velocity by 4 cm s^{-1} (Fig. 12). Therefore, benthic assemblages and grain-size data support the presence of an active Levantine Intermediate Water (LIW) during MIS 2 in the Gela Basin, impacting the benthic communities, in agreement with the intense Mediterranean thermohaline circulation recorded in the Western Mediterranean Sea for the same time interval (e.g. Sierro et al., 2005; Cacho et al., 2007).

During the lower phase of HS1 (18–16.3 kyr BP), the $\overline{SS}$ constantly decreases although still indicates fast bottom-currents (Fig. 12). Planktonic assemblages are still representative of cold and productive water (PI 1b, Table 3), whereas benthic assemblages are dominated by infaunal species resistant to low oxygen conditions (e.g. De Rijk et al., 1999; Goineau et al., 2012) (Be 1b in Table 3). In particular, the *B. marginata* $\delta^{13}C_{forams}$ shows a slight increase of the mean values in comparison with the previous interval. This trend may suggest a decrease of organic flux to the seafloor. In fact, a change in the microhabitat by *B. marginata* as response to variations of oxygen/food supply (e.g., vertical migration towards the sediment-water interface, Jorissen et al., 1995) is not plausible, because the benthic assemblage does not show major changes in the most abundant/dominant taxa between ecozones (Be 1a and Be 1b in Table 3). More importantly, the observed $\delta^{13}C$ increase does not match with the general abrupt decreasing trend, which starts at 18 ka and culminates during the HE1 event, displayed by the $\delta^{13}C$ record of the epibenthic taxa *C. pachyderma* in the western Mediterranean Sea (Cacho et al., 1999, 2007), Menorca drift (Sierro et al., 2005) and Strait of Sicily (Vergnaud-Grazzini et al., 1988) (Fig. 11). Therefore, the progressive weakening of the Western Mediterranean Deep Water (Cacho et al., 1999, 2007; Sierro et al., 2005) and slowdown of the vertical mixing of water masses in the Strait of Sicily (Vergnaud-Grazzini et al., 1988) is not registered in the high-resolution sedimentary record of core MS72 with the same intensity and pace during this time interval.

During the upper phase of HS1 (16.3–15 kyr BP) the $\delta^{13}C$ of *B. marginata* and *G. bulloides* finally start showing a marked decreasing trend just below the $\delta^{18}O$ minimum peak related to the HE1 event (Fig. 11), pointing to enhanced water mass stratification and productivity, in agreement with increased Ba/Ti (Fig. 10). The $\overline{SS}$ further

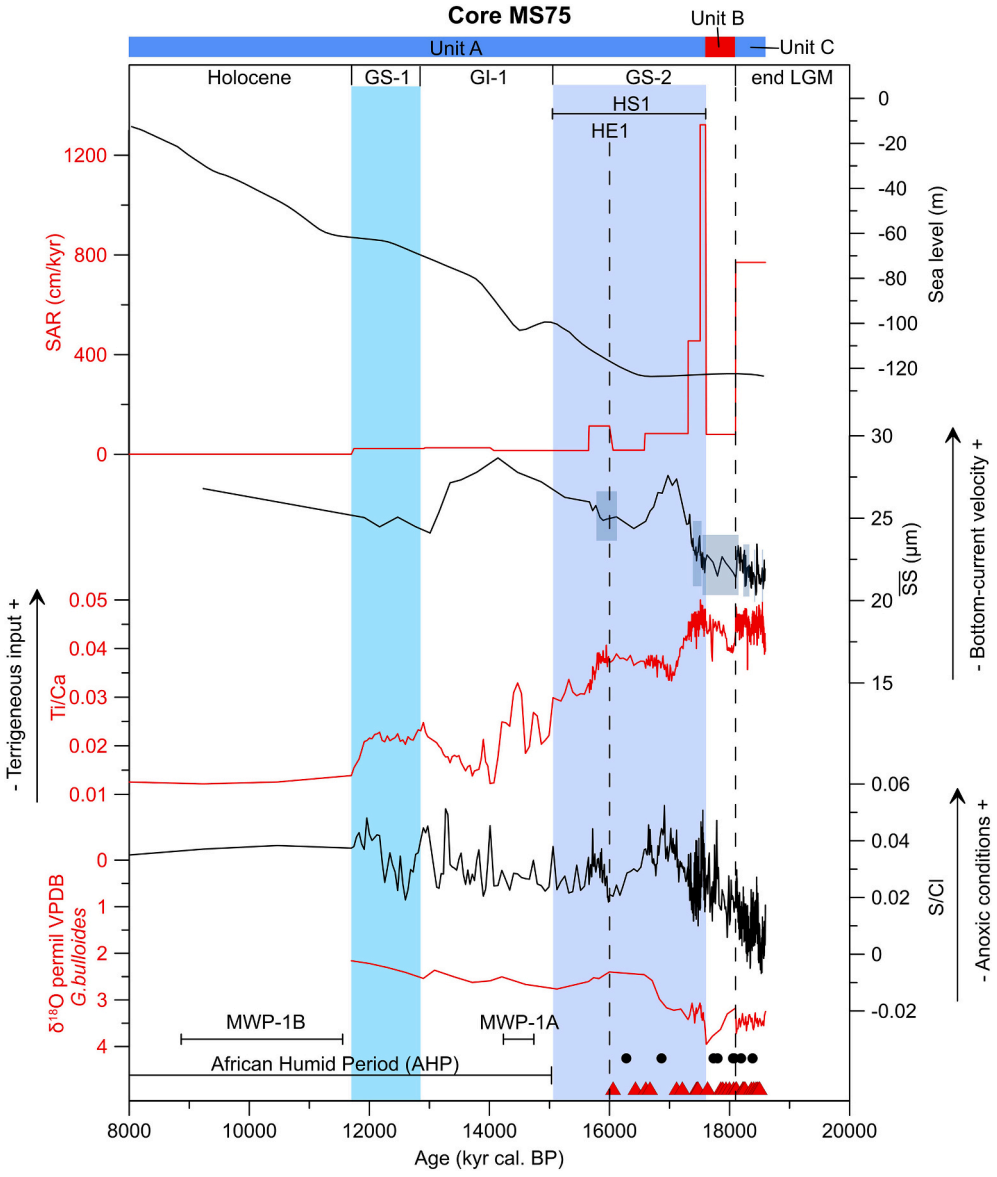

Fig. 9. Isotopic stratigraphy ($\delta^{18}O$), geochemical element composition (S/Cl, Ca/Ti), sortable silt mean size ($\overline{SS}$) and LSR of core MS75 displayed in age. Sea-level curve from Lambeck et al. (2014). Reworked foraminifera = black circles, pyrites = red triangles. GS-1 = Glacial Stadial 1 (sky blue bar), GI-1 = Glacial Interstadial 1, HS1 = Heinrich Stadial 1 (dark blue bar), HE1 = Heinrich Event 1, LGM = Last Glacial Maximum. Pale blue rectangles on $\overline{SS}$ data represent sediments unsorted by bottom currents. (For interpretation of the references to colour in this figure legend, the reader is referred to the web version of this article.)

decreases highlighting an overall decreasing in current speed of 6 cm s^{-1} since the base of the HS1 (Fig. 12). Transitional ichnofacies appear around HE1 (Fig. 4C), suggesting a change to intermediate ventilation and reduced stress at the seafloor. Overall, the data suggest that only in the late HS1 the Gela Basin slope was progressively affected by the weakening of the bottom currents accompanied by increase of water stratification and organic flux to the sea-bottom, in agreement with similar observations in the Western Mediterranean (Cacho et al., 2007) and Strait of Sicily (Vergnaud-Grazzini et al., 1988) (Fig. 1). However, this slow-down is in striking contrast with observations made in the Corsica Trough where the LIW's speed increases during HE1 in association with minimal sea-surface temperatures recorded throughout the Mediterranean Sea (Toucanne et al., 2012, Fig. 12). The stratigraphically-expanded sedimentary succession of the Gela Basin thus reveals, for the first time, the short-term variability of the LIW in the Central Mediterranean Sea during HS1. Our data suggest that the decisive weakening of the LIW began 16.3–16.5 kyr BP, ca. 1000 years before what has been previously suggested by Toucanne et al. (2012) and does not coincide with the amelioration of the atmospheric circulation at the beginning of the interstadial (i.e. GI-1 warm period). This difference can be the result of small-scale oceanographic differences in circulation pattern between the Corsica Trough and Gela Basin, which can be ascribed both to the quite different morphological settings and the connection with the Western Mediterranean. The Corsica Trough consists of a linear narrow corridor well connected with the surface circulation of the Western Mediterranean, to whose changes responds promptly. On the other hand, the Gela Basin is a bowl-shaped basin, which better reflects the oceanographic changes of the eastern Mediterranean and in particular the LIW's dynamics. In summary, our sediment cores seem capable of better disentangling the different circulation patterns between the Western and the Eastern Mediterranean at a centennial time-scale.

Subsequently, during the Greenland Interstadial 1 (GI-1, 15 kyr–12.8 kyr cal. BP) $\delta^{18}O$ show trends similar to the rest of the Mediterranean (e.g. Desprat et al., 2013, Fig. 11), $\overline{SS}$ data indicate the continued weakening of the LIW on the lower slope. The concurrent drastic Ti/Ca drop associated with very low LSR support low lateral advection during Gl-1, resulting in the deposition of sediments relatively high in biogenic Ca on the lower slope. These overall conditions are in agreement with observations made in the reference studies (Fig. 12). On the contrary, $\overline{SS}$ data of core MS75 show a large increase of the flow velocities from 16.5 ka (+5.7 cm s^{-1}, Fig. 12). This large flow increase is supported by grain-size

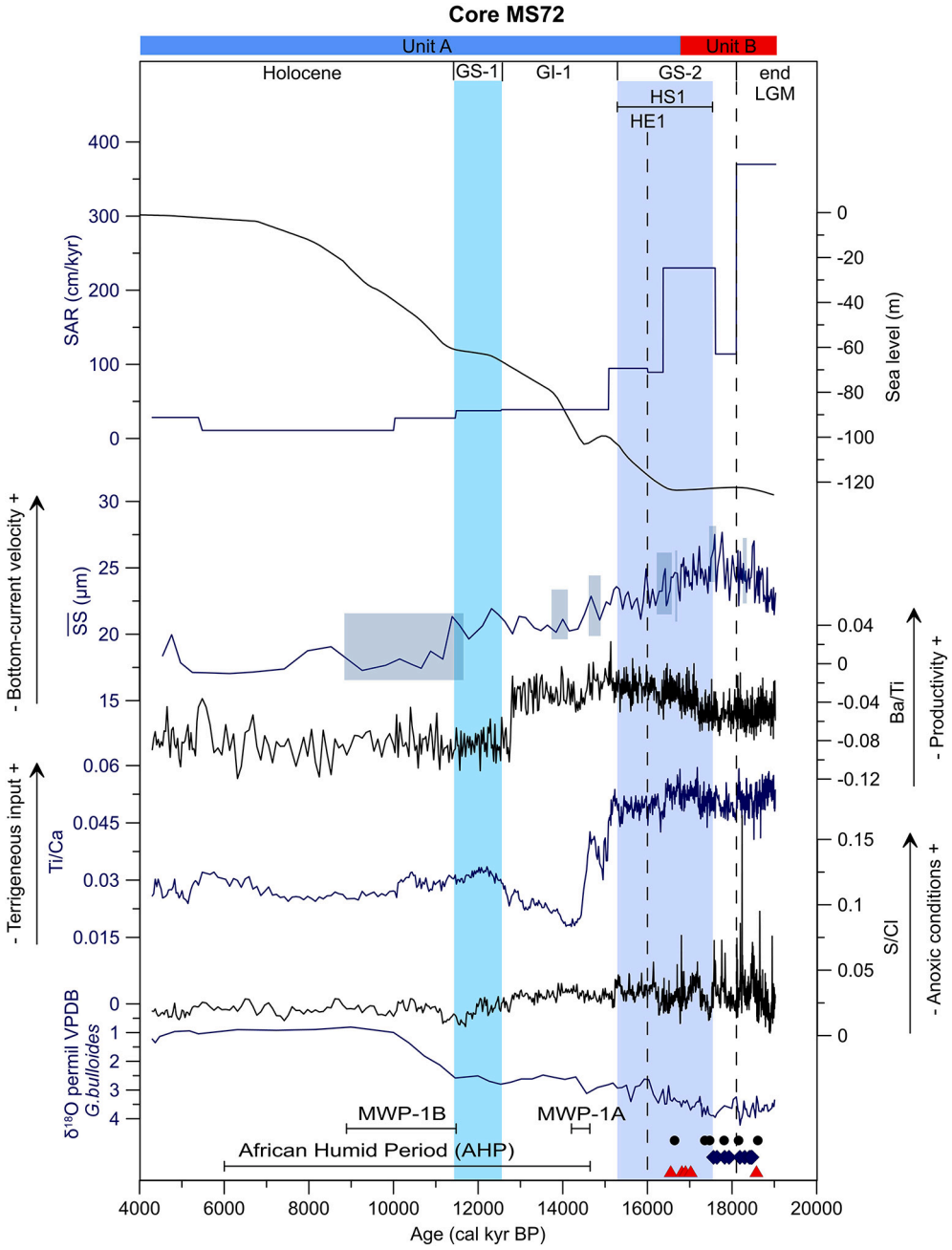

Fig. 10. Isotopic stratigraphy ($\delta^{18}O$), geochemical element composition (S/Cl, Ca/Ti, Ba/Ti), sortable silt mean size ($\overline{SS}$), and LSR of core MS72 displayed in age. Sea-level curve from Lambeck et al. (2014). Reworked foraminifera = black circles, pyrites = black triangles, plant debris = blue diamonds. See Fig. 9 for other symbols and abbreviations. (For interpretation of the references to colour in this figure legend, the reader is referred to the web version of this article.)

bimodal distribution, inverse to normal grading and high Zr/Rb (Fig. 3B), which constrain the activity of a current able to mobilize coarse grains on the upper slope. Active bottom currents are also shown by increasing presence of micro-ichnofacies indicative of stressful conditions at the seafloor (Fig. 3D). Overall, Gl-1 marks an abrupt warming associated with an extremely rapid sea-level rise up to 20 m between 14.3 and 12.8 ka caused by Meltwater Pulse-1A (Stanford et al., 2011, Fig. 9). The widened cross-section of the Strait of Gibraltar promotes Atlantic freshwater discharge with consequent salinity decrease of the Mediterranean Sea (Rogerson et al., 2012). We thus suggest an upward vertical shift of the LIW during GI-1 in response to enhanced water column density gradient, caused by the presence of dense Atlantic water masses at shallower depths and surface freshening in the Mediterranean. Supporting the idea of a lighter LIW during sea-level rise, the $\delta^{18}O$ *G. bulloides* signal shows progressive depletion around mid GI-1 in the Gela Basin (Fig. 7). Indeed, sea-level variations seem capable of controlling the buoyancy of saline waters, as for example in the Gulf of Cádiz, where the density gradient promoted the Mediterranean Outflow Water (MOW) shoaling during the last deglaciation (Jiménez-Espejo et al., 2015) while increased salinity during sea-level lowstands might have produced a downslope shift of a denser MOW (Kaboth et al., 2015). Furthermore, the onset of the African Humid Period (AHP) around the same time may have added another forcing that hampered the ventilation in the Eastern Mediterranean, which would concur to explain the drastic reduction of the density of the LIW on the lower slope of the Gela Basin. On the same line of reasoning, Toucanne et al. (2012) notice the progressive shoaling of the LIW from 20 to 12 ka in the Corsica Trough, they interpret the benthic $\delta^{18}O$ record as reflecting significant density

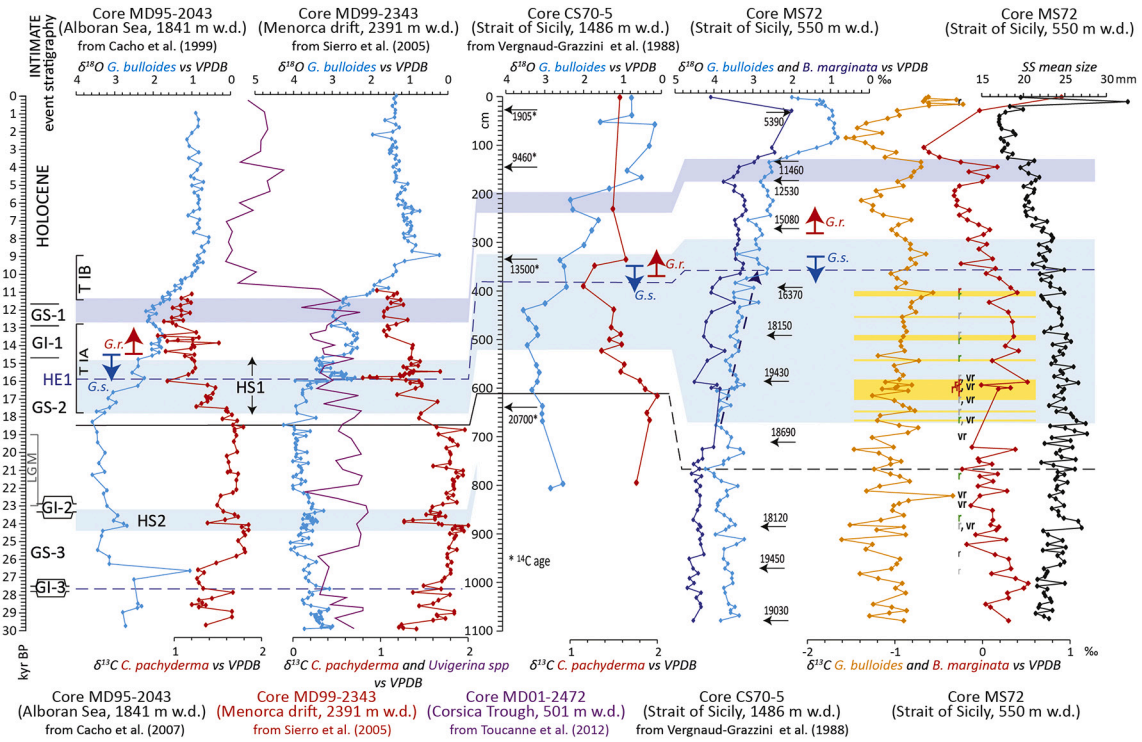

Fig. 11. Basin-wide correlation of benthonic and planktonic $\delta^{13}C$ and $\delta^{18}O$ records of core MS72 and the reference cores of the Mediterranean (see references on top of each core). The ages are calibrated (yr BP). The yellow stripes represent the intervals with evidence of major reworking/displacement of foraminifera. See Fig. 7 for a detailed explanation of symbols and abbreviations. (For interpretation of the references to colour in this figure legend, the reader is referred to the web version of this article.)

changes of the LIW in relation to climate stadial/interstadial cycles (Toucanne et al., 2012). However, sedimentary records in the Corsica Trough have no sufficient resolution during HS1 and are located only in the deeper part of the basin and are thus not ideal to highlight different bottom-current behaviours along different depths of the slope. The $\overline{SS}$ data of core MS75 indicate that reconstructed paleo-flow velocities drastically decrease starting from 12.8 kyr BP when the return of the domination of *G. bulloides* and *N. incompta* with the rare presence of *G. ruber* mark the inception of the Greenland Stadial 1 (GS-1) at ca. 12.65–12.9 kyr BP. The appraisal of cooler temperatures is reflected also by rapid Ti/Ca increase observed in both cores, most probably related to the attenuated biogenic activity. We thus possibly constrain the timing of the shoaling phase of the LIW between 16.5 and 12.8 ka in the Gela Basin, which coincides with the time interval of enhanced sea-level rise (Fig. 12).

Finally, during GS-1, significant intensification of the LIW activity has been observed in the Mediterranean (e.g. McCulloch et al., 2010) and particularly in the Corsica Trough (Fig. 12). On the contrary, slight increases of $\overline{SS}$ in core MS72 and even more subtle in core MS75 (Fig. 12) suggest smaller bottom-current acceleration in the Gela Basin. Comparing the depths of the sediment cores collected in the Gela Basin and Corsica Trough with bottom-current velocities, we infer that the LIW was flowing at maximum speed between 210 and 430 m wd in the Gela Basin (Fig. 12), possibly in relation to the pause in sea-level rise during GS-1.

5.3. Predisposing conditions to slope instability

The multi-proxy sedimentary records of the Gela Basin allow to better constraining the timing of erosion/deposition along the shelf edge and the identification of conditions that promote failure of drifts deposits.

Around 16.5 ka planktonic taxa characteristic of MIS 5 or older (*G. truncatulinoides*) are present in sediment core MS72 (red "r" in Fig. 7), suggesting the reworking of sediments trough MTDs. Our data show that two submarine landslides, the South Gela Basin Slides (SGBS) and the Gela Drift Slide (GDS) have been emplaced around the same time interval from the wasting of sediment drifts that were growing since MIS 5 (Gauchery et al., 2021).

Shortly before, between 17.5 and 17 ka, a short-living but decisive increase in bottom-current strength in the upper slope and shelf-edge area is constrained by reliable data for paleo-flow reconstructions of core MS75 (Fig. 9). The increase in flow velocity is accompanied by LSR peaking to 1320 cm/kyr (ca. 17.5–17.2 ka) and plummeting soon after, when velocities reach their maximum speed. Furthermore, the velocity increase mirrors the drastic decrease in Ti/Ca, which can be related to the sudden change in the strength of lateral advection in the upper slope (Figs. 9, 12). This brief episode of acceleration appears disjointed by sea-level variations and climate forcing, because sea level was steadily rising by 12 cm/kyr during this time interval (Lambeck et al., 2014) and is uncoupled from the activity and dynamics of the LIW. We therefore suggest that sediment remobilization is related to the action of bottom currents under the influence of the surface water mass (MAW). On the other hand, the presence of bottom currents displacing sediments on the outer shelf and constrained in their paths by the structural highs of the Malta Plateau during flooding phases was already hypothesized by Gauchery et al. (2021), based on geophysical data only. Therefore, we suggest that the MAW accelerated along the shelf of the Gela Basin at the beginning of deglaciation in combination with local topographic constraints on the shelf. The erosion of the outer shelf may have been enhanced by the action of storm waves compatible with the path of atmospheric circulation characterized by southerlies during LGM (Kuhlemann et al., 2008).

Storm waves and bottom currents, the latter governed by surface-water circulation, triggered the instability of the contourite drifts that at the time were as shallow as 100 m water depth. In the literature,

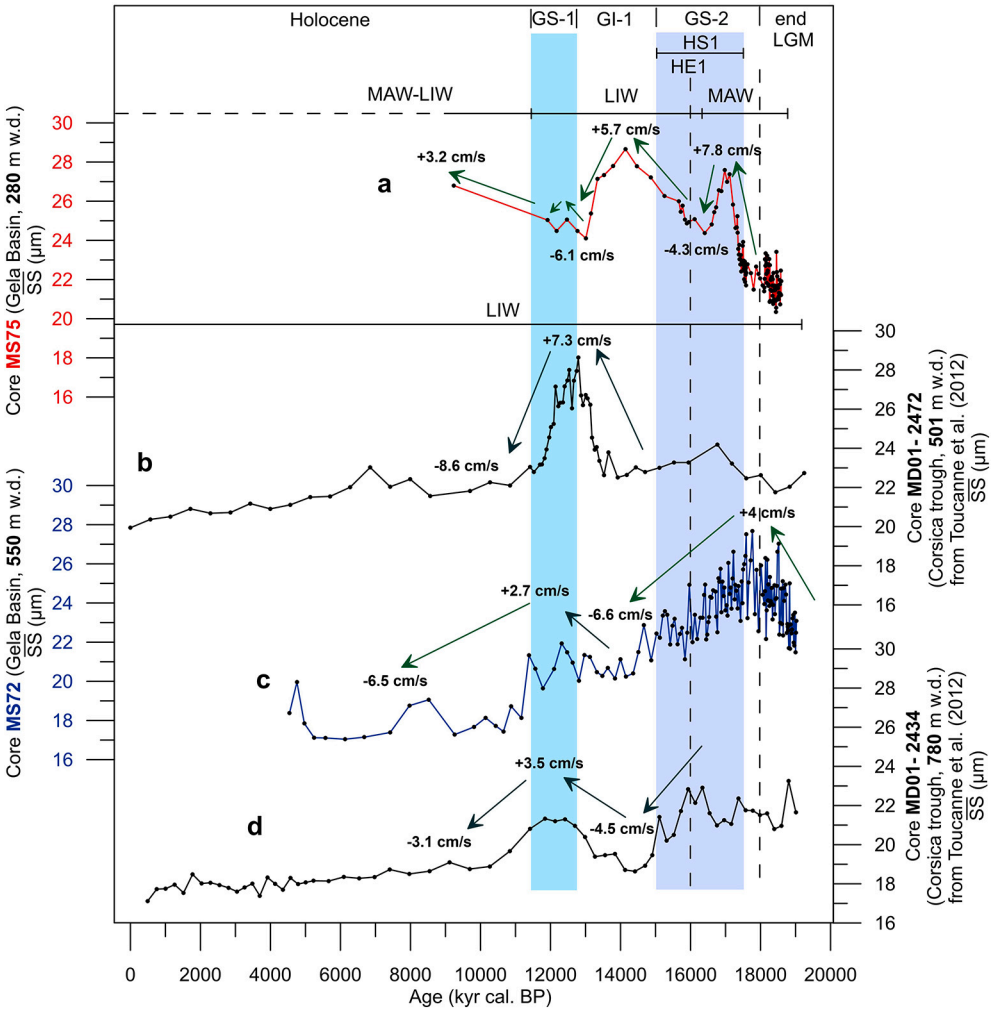

Fig. 12. Sortable silt mean size ($\overline{SS}$) in the Gela Basin (A and C) compared to the Corsica Trough (B and D) over the last 19 kyr BP. The green arrows indicate the increases and decreases in flow speed (cm s^{-1}). The deepest cores (all but MS75) registered fluctuations of the intermediate water mass (LIW). The shallower core (MS75) shows contrasting values compared to the other cores, which possibly reflect changes in the depth of the upper boundary of the LIW due to sea-level rise pulses and the activity of the surface water (MAW) at the beginning of deglaciation. (For interpretation of the references to colour in this figure legend, the reader is referred to the web version of this article.)

several reasons are identified to explain the occurrence of failure in contourite deposits, including the oversteepening caused by the mounded geometry itself and the high sedimentation rates in well-sorted sediments that promote overloading combined with low shear strength (e.g. Rebesco et al., 2014). Furthermore, seismic triggering has been excluded for the specific case of SGBS based on the margin stability analysis carried out with the minimum lithostatic deviation method which accounts for peak ground acceleration estimated along the continental margin (see Zaniboni et al., 2021). We thus suggest that a further predisposing condition to failure for shallow-water contourites is provided by rapid changes of bottom-current velocities in the upslope of contourite drifts.

Another increase (+3.2 cm s^{-1}) of the flow velocity (Fig. 12), accompanied by high Zr/Rb (Fig. 9), is visible in core MS75 after the end of GS-1. The increase lasts until the core top, which is chronologically constrained at 8 kyr cal. BP. The velocity increase is associated with a continuous decrease of the sedimentation rate from the early Holocene (Fig. 9). This further increase in bottom current activity in the upper slope is timely related to the discharge of Atlantic freshwater during Meltwater Pulse-1B, which was a multi-millennial interval of enhanced rates of sea-level rise between 11.5 ka and 8.8 ka BP (Stanford et al., 2011). This prolonged freshwater discharge may have induced significant differences in density between the surface and intermediate water masses with the creation of internal waves oscillating along the interface between the LIW and the MAW. Internal waves are capable of sediment mobilization in shallow slope settings and promote long-term downslope transport (e.g. Ma et al., 2016). The sediment hiatus corresponding to the last 8 kyr BP suggests that erosion may have taken place in the upper slope seafloor of the Gela Basin as also revealed by the seismic facies of the sub-bottom profiles (Fig. 3A). The slight increase of current strengths in the upper slope may have promoted seabed erosion in the southern Gela Basin in the early Holocene, which is around the time when mudflows were emplaced (ca. 8.5 ka) in the northern Gela Basin (Kuhlmann et al., 2017). This would infer that changes in sea level and variations in water-mass interface may favour erosion of the shelf edge and upper slope and can contribute to the instability of shallow-water contourite drifts.

6. Conclusions

Extensive sediment drifts developed on the upper and lower slope of Gela Basin, in the Strait of Sicily, which is a topographically complex region that allows surface and intermediate water exchange between the eastern and the western Mediterranean basins. Two sediment cores span the post-LGM and are characterized by exceptionally high sedimentation rates in the last phase of LGM and the early Heinrich Stadial 1 (~19 kyr–16 kyr BP) that provide an excellent record to reconstruct the fine-scale variability of the paleoceanographic circulation and sedimentary processes in the Central Mediterranean. The multi-proxy sedimentary records allow to: 1) distinguish sedimentary processes controlled by along-slope currents from downslope sediment-gravity flows; 2) reconstruct the variability of the paleo-current activity and intensity in relation to sea-level fluctuations; 3) identify genetic links between contourite deposits and MTDs suggesting key time intervals and

predisposing conditions that lead to the failure of part of the sediment drifts. In particular, the expanded sedimentary records allowed us to perform a semi-quantitative analysis of displaced foraminifera and stranded plant debris in sediment layers, which were not defined as current-sorted by the sortable silt method, to diagnose downslope sedimentary processes.

During the post-LGM lowstand and first phases of sea-level rise, sediment was supplied to the lower slope from the inner-middle shelf, where erosion was caused by storm waves and/or bottom currents. Strong intermediate water bottom-currents caused lateral advection from north to south and enhanced sediment accumulation in the mid-lower slope. Here, the sedimentary facies show an overprinting of lateral traction transport and sediment load structures proving the concurrent presence of along-slope and downslope processes active at the same time. This implies that sediment fluxes from land are not necessarily accountable for high sedimentation rates on margins dominated by intense bottom-water circulation.

The stratigraphically-expanded sedimentary succession of the Gela Basin allowed predating the progressive weakening of the Levantine Intermediate Water (LIW) at 16.3 kyr BP. Thus, the LIW slow-down seems independent of climate forcing related to atmospheric temperatures and position of the northern polar fronts, contrary to what was previously suggested from core sediment evidence in the Corsica Through, in the Central Mediterranean. Rather, the slow-down of the LIW was affiliated with sea-level rise pulses, consequent increased Atlantic fresh water discharge at the Strait of Gibraltar and Mediterranean surface freshening. In particular, the change in salinity gradient caused the progressive shoaling of the LIW upper boundary between 16.5 and 12.8 ka. Thus, sea-level fluctuations have a direct impact on the buoyancy of the bottom-currents inducing density gradients that may change the depth interface of water masses and therefore their capability of mobilizing sea-bottom sediments.

The action of persisting bottom currents in the upslope of shallow-water sediment drifts, driven by surface water masses that respond to sea-level fluctuations, combined with drastic changes in sedimentation rates, seem to create predisposing conditions to the failure of sediment drifts. In the Gela Basin, in particular, enhanced instability of sediment drifts that accumulated since the previous interglacial period occurred during two key-time intervals. 1) The lower phase of HS1, around 17 ka, when brief acceleration of wind-driven water masses and storm waves caused erosion on the outer shelf; 2) the early Holocene, when prolonged sea-level rise and freshwater discharge caused changes in density at the interface between the Modified Atlantic Water and the Levantine Intermediate Water, which promoted sediment erosion and downslope transport.

Data availability

Bathymetric data used in this research work are downloadable from the EMODnet compilation at https://portal.emodnet-bathymetry.eu/. All other raw and processed data such as core photos, X-ray images of the cores and grain-size analysis are available upon request to the corresponding author.

Declaration of Competing Interest

The authors declare that they have no known competing financial interests or personal relationships that could have appeared to influence the work reported in this paper.

Acknowlegments

The first author wishes to thank Samuel Toucanne for the raw sediment core data of the Corsica Trough used in Fig. 12 and for the guidance on the methodology of the grain-size analysis. Grain-size analyses were performed at Ifremer during TG's several stays (secondments) within the SLATE project. We thank Jeremie Gouriou for his kind assistance in the sedimentology laboratory. Authors are grateful to two anonymous reviewers for their valuable comments. The PhD of Tugdual Gauchery was funded by the European Union's Horizon 2020 research and innovation programme under the Marie-Skłodowska-Curie grant via project ITN SLATE (grant agreement N° 721403).

References

Argnani, A., 1987. The Gela nappe: evidence of accretionary melange in the maghrebian foredeep of sicily. Memorie Societ'a Geologica Italiana 38, 419–428.

Ariztegui, D., Asioli, A., Lowe, J.J., Trincardi, F., Vigliotti, L., Tamburini, F., Chondrogianni, C., Accorsi, C.A., Bandini Mazzanti, M., Mercuri, A.M., Van der Kaars, S., McKenzie, J.A., Oldfield, F., 2000. Paleoclimate and the formation of sapropel S1: inferences from late Quaternary lacustrine and marine sequences in the Central Mediterranean region. Palaeoceanogr. Palaeoclimatol. Palaeoecol. 158, 215–240. https://doi.org/10.1016/S0031-0182(00)00051-1.

Asioli, A., Trincardi, F., Lowe, J.J., Oldfield, F., 1999. Short-term climate changes during the last Glacial–Holocene transition: comparison between Mediterranean records and the GRIP event stratigraphy. J. Quat. Sci. 14, 373–381. https://doi.org/10.1002/(SICI)1099-1417(199907)14:4<373::AID-JQS472>3.0.CO;2-T.

Asioli, A., Trincardi, F., Lowe, J.J., Ariztegui, D., Langone, L., Oldfield, F., 2001. Submillennial scale climatic oscillations in the central Adriatic during the Late glacial: palaeoceanographic implications. Quat. Sci. Rev. 20, 1201–1221. https://doi.org/10.1016/S0277-3791(00)00147-5Get.

Astraldi, M., Balopoulos, S., Candela, J., Font, J., Gacic, M., Gasparini, G.P., Manca, B., Theocharis, A., Tintoré, J., 1999. The role of straits and channels in understanding the characteristics of Mediterranean circulation. Prog. Oceanogr. 44 (1–3), 65–108. https://doi.org/10.1016/S0079-6611(99)00021-X.

Astraldi, M., Gasparini, G.P., Gervasio, L., Salusti, E., 2001. Dense water dynamics along the Strait of Sicily (Mediterranean Sea). J. Phys. Oceanogr. 31, 3457–3475. https://doi.org/10.1175/1520-0485(2001)031<3457:DWDATS>2.0.CO;2.

Bahr, A., Jiménez-Espejo, F., Kolasinac, N., Grunert, P., Hernández-Molina, F., Röhl, U., Voelker, A., Escutia, C., Stow, D., Hodell, D., Zarikian, C., 2014. Deciphering bottom current velocity and paleoclimate signals from contourite deposits in the Gulf of Cádiz during the last 140 kyr: an inorganic geochemical approach. Geochem. Geophy. Geosy. 15 https://doi.org/10.1002/2014GC005356.

Beckers, A., Beck, C., Hubert-Ferrari, A., Tripsanas, E., Crouzet, C., Sakellariou, D., Papatheodorou, G., De Batist, M., 2016. Influence of bottom currents on the sedimentary processes at the western tip of the Gulf of Corinth, Greece. Mar. Geol. 378, 312–332. https://doi.org/10.1016/j.margeo.2016.03.001.

Béranger, K., Mortier, L., Gasparini, G.P., Gervasio, L., Astraldi, M., Crépon, M., 2004. The dynamics of the Sicily Strait: a comprehensive study from observations and models. Deep-Sea Res. Pt. II 51 (4–5), 411–440. https://doi.org/10.1016/j.dsr2.2003.08.004.

Björck, S., Walker, M.J.C., Cwynar, L., Johnsen, S.J., Knudsen, K.L., Lowe, J.J., Wohlfarth, B., 1998. An event stratigraphy for the last termination in the North Atlantic region based on the Greenland Ice Core record: a proposal by the INTIMATE group. J. Quat. Sci. 13, 283–292. https://doi.org/10.1002/(SICI)1099-1417(199807/08)13:4<283::AID-JQS386>3.0.CO;2-A.

Blockley, S.P.E., Lane, C.S., Hardiman, M., Rasmussen, S., Seierstad, I., Steffensen, J.P., Svensson, A., Lotter, A.F., Turney, C.S., Ramsey, C.B., 2012. Synchronisation of palaeoenvironmental records over the last 60,000 years, and an extended INTIMATE event stratigraphy to 48,000 b2k. Quat. Sci. Rev. 36, 2–10. https://doi.org/10.1016/j.quascirev.2011.09.017.

Bond, G., Bond, G.C., Heinrich, H., Broecker, W., Labeyrie, L., McManus, J., Andrews, J., Huon, S., Jantschik, R., Clasen, S., Simet, C., Tedesco, K., Klas, M., Bonani, G., Ivy, S., 1992. Evidence for massive discharges of icebergs into the glacial northern Atlantic. Nature 360, 245–249. https://doi.org/10.1038/360245a0.

Brackenridge, R.E., Hernández-Molina, F.J., Stow, D.A.V., Llave, E., 2013. A Pliocene mixed contourite-turbidite system offshore the Algarve margin, Gulf of Cadiz: Seismic response, margin evolution and reservoir implications. Mar. Pet. Geol. 46, 36–50. https://doi.org/10.1016/j.marpetgeo.2013.05.015.

Cacho, I., Grimalt, J.O., Pelejero, C., Canals, M., Sierro, F.J., Flores, J.A., Shackleton, N. J., 1999. Dansgaard-Oeschger and Heinrich event imprints in the Alboran Sea paleotemperatures. Paleoceanography 14, 698–705. https://doi.org/10.1029/1999PA900044.

Cacho, I., Grimalt, J.O., Canals, M., Sbaffi, L., Shackleton, N.J., Schönfeld, J., Zahn, R., 2001. Variability of the western Mediterranean Sea surface temperature during the last 25,000 years and its connection with the northern hemisphere climatic changes. Paleoceanography 16, 40–52. https://doi.org/10.1029/2000PA000502.

Cacho, I., Shackleton, N., Elderfield, H., Sierro, F., Grimalt, J., 2007. Glacial rapid variability in deep-water temperature and δ 18O from the Western Mediterranean Sea. Quat. Sci. Rev. 25, 3294–3311. https://doi.org/10.1016/j.quascirev.2006.10.004.

Cornuault, M., Tachikawa, K., Vidal, L., Guihou, A., Siani, G., Deschamps, P., Bassinot, F., Revel, M., 2018. Circulation changes in the eastern Mediterranean Sea over the past 23,000 years inferred from authigenic Nd isotopic ratios. Paleoceanogr. Paleoclimatol. 33, 264–280. https://doi.org/10.1002/2017PA003227.

De Rijk, S., Troelstra, S.R., Rohling, E.J., 1999. Benthic foraminiferal distribution in the Mediterranean Sea. J. Foram. Res. 29, 93–103. https://doi.org/10.2113/gsjfr.29.2.93.

De Stigter, H.C., Jorissen, F.J., Van der Zwaan, G.J., 1998. Bathymetric distribution and microhabitat partitioning of live (Rose Bengal stained) benthic foraminifera along a shelf to deep sea transect in the southern Adriatic Sea. J. Foram. Res. 28, 40–65.
DeLaune, R.D., Lindau, C.W., 1987. $\delta^{13}C$ signature of organic carbon in estuarine bottom sediment as an indicator of carbon export from adjacent marshes. Biogeochemistry 3, 225–230.
Deschamps, P., Durand, N., Bard, E., Hamelin, B., Camoin, G., Thomas, A.L., Henderson, G.M., Okuno, J., Yokoyama, Y., 2012. Ice-sheet collapse and sea-level rise at the Bølling warming 14,600 years ago. Nature 483, 559–564. https://doi.org/10.1038/nature10902.
Desprat, S., Combourieu-Nebout, N., Essallami, L., Sicre, M.A., Dormoy, I., Peyron, O., Siani, G., Bout Roumazeilles, V., Turon, J.L., 2013. Deglacial and Holocene vegetation and climatic changes in the southern Central Mediterranean from a direct land-sea correlation. Clim. Past 9, 767–787. https://doi.org/10.5194/cp-9-767-2013.
Dorador, J., Tovar, F., Mena, A., Francés, G., 2019. Lateral variability of ichnological content in muddy contourites: Weak bottom currents affecting organisms' behavior. Sci. Rep. 9, 17713. https://doi.org/10.1038/s41598-019-54246-3.
Dubois-Dauphin, Q., Montagna, P., Giuseppe, S., Douville, E., Wienberg, C., Hebbeln, D., Liu, Z., Kallel, N., Dapoigny, A., Revel Pons-Branchu, E., Taviani, M., Colin, C., 2017. Hydrological variations of the intermediatewater masses of the western Mediterranean Sea during the past 20 ka inferred from neodymium isotopic composition in foraminifera and cold-water corals. Clim. Past 13, 17–37. https://doi.org/10.5194/cp-2016-64.
EMODnet Bathymetry Consortium, 2016. EMODnet Digital Bathymetry (DTM). The European Marine Observation and Data Network. https://doi.org/10.12770/c7b53704-999d-4721-b1a3-04ec60c87238.
Ferraro, S., Sulli, A., Di Stefano, E., Giaramita, L., Incarbona, A., Graham Mortyn, P., Sprovieri, M., Sprovieri, R., Tonielli, R., Vallefuoco, M., Zizzo, E., Tranchida, G., 2018. Late Quaternary palaeoenvironmental reconstruction of sediment drift accumulation in the Malta Graben (Central Mediterranean Sea). Geo-Mar. Lett. 38, 241–258. https://doi.org/10.1007/s00367-018-0534-x.
Fonnesu, M., Palermo, D., Galbiati, M., Marchesini, M., Bonamini, E., Bendias, D., 2020. A new world-class deep-water play-type, deposited by the syndepositional interaction of turbidity flows and bottom currents: the giant Eocene Coral Field in northern Mozambique. Mar. Pet. Geol. 111, 179–201. https://doi.org/10.1016/j.marpetgeo.2019.07.047.
Gauchery, T., Rovere, M., Pellegrini, C., Cattaneo, A., Campiani, E., Trincardi, F., 2021. Factors controlling margin instability during the Plio-Quaternary in the Gela Basin (Strait of Sicily, Mediterranean Sea). Mar. Petrol. Geol. 123, 104767 https://doi.org/10.1016/j.marpetgeo.2020.104767.
Ghielmi, M., Amore, M.R., Bolla, E.M., Carubelli, P., Knezaurek, G., Serraino, C., 2012. The Pliocene to pleistocene succession of the hyblean foredeep (sicily, Italy). October 23–26, 2011. In: AAPG (Am. Assoc. Pet. Geol.) Internat. Conf. Exhib. Milan, Italy. http://www.searchanddiscovery.com/documents/2012/30220ghielmi/ndx_ghielmi.pdf.
Goineau, A., Fontanier, C., Jorissen, F., Buscail, R., Kerhervé, P., Cathalot, C., Pruski, A. M., Lantoine, F., Bourgeois, S., Metzger, E., Legrand, E., Rabouille, C., 2012. Temporal variability of live (stained) benthic foraminiferal faunas in a river-dominated shelf – Faunal response to rapid changes of the river influence (Rhône prodelta, NW Mediterranean). Biogeosciences 9, 1367–1388. https://doi.org/10.5194/bg-9-1367-2012.
Govin, A., Holzwarth, U., Heslop, D., Ford Keeling, L., Zabel, M., Mulitza, S., Collins, J. A., Chiessi, C.M., 2012. Distribution of major elements in Atlantic surface sediments (36°N-49°S): imprint of terrigenous input and continental weathering. Geochem. Geophys. Geosyst. 13, 1–23. https://doi.org/10.1029/2011GC003785.
Hanebuth, T., Zhang, W., Hofmann, A., Löwemark, L., Schwenk, T., 2015. Oceanic density fronts steering bottom-current induced sedimentation deduced from a 50 ka contourite-drift record and numerical modeling (off NW Spain). Quat. Sci. Rev. 112, 207–225. https://doi.org/10.1016/j.quascirev.2015.01.027.
Heinrich, H., 1988. Origin and consequences of cyclic ice rafting in the Northeast Atlantic Ocean during the past 130,000 years. Quat. Res. 29, 142–152. https://doi.org/10.1016/0033-5894(88)90057-9.
Hennekam, R., De Lange, G., 2012. X-ray fluorescence core scanning of wet marine sediments: methods to improve quality and reproducibility of high-resolution paleoenvironmental records. Limnol. Oceanogr. Methods 10, 991–1003. https://doi.org/10.4319/lom.2012.10.991.
Hernandez-Molina, F.J., Llave, E., Preu, B., Ercilla, G., Fontan, A., Bruno, M., Serra, N., Gomiz, J.J., Brackenridge, R.E., Sierro, F.J., Stow, D.A.V., García, M., Juan, C., Sandoval, N., Arnaiz, A., 2014. Contourite processes associated to the Mediterranean Outflow Water after its exit from the Strait of Gibraltar: Global and conceptual implications. Geology 42 (3), 227–230. https://doi.org/10.1130/G35083.1.
Hodell, D.A., Nicholl, J.A., Bontognali, T.R.R., Danino, S., Dorador, J., Dowdeswell, J.A., Einsle, J., Kuhlmann, H., Martrat, B., Mleneck-Vautravers, M.J., Rodríguez-Tovar, F. J., Röhl, U., 2017. Anatomy of Heinrich Layer 1 and its role in the last deglaciation. Paleoceanogr. 32, 284–303. https://doi.org/10.1002/2016PA003028.
Jaccard, S.L., Galbraith, E.D., Sigman, D.M., Haug, G.H., 2010. A pervasive link between Antarctic icecore and subarctic Pacific sediment records over the past 800 kyrs. Quat. Sci. Rev. 29, 206–212. https://doi.org/10.1016/j.quascirev.2009.10.007.
Jiménez-Espejo, F.J., Pardos-Gené, M., Martínez-Ruiz, F., García-Alix, A., van de Flierdt, T., Toyofuku, T., Bahr, A., Kreissig, K., 2015. Geochemical evidence for intermediate water circulation in the westernmost Mediterranean over the last 20 kyr BP and its impact on the Mediterranean Outflow. Glob. Planet. Change 135, 38–46. https://doi.org/10.1016/j.gloplacha.2015.10.001.
Jorissen, F.J., 1987. The distribution of benthic foraminifera in the Adriatic Sea. Mar. Micropaleontol. 12, 21–48.
Jorissen, F.J., 1999. Benthic foraminiferal microhabitats below the sediment-water interface. In: Sen Gupta, B.K. (Ed.), Modern Foraminifera. Kluwer Academic Publishers, Great Britain, pp. 161–179. https://doi.org/10.1007/0-306-48104-9_10.
Jorissen, F.J., de Stigter, H.C., Widmark, J.G.V., 1995. A conceptual model explaining benthic foraminiferal microhabitats. Mar. Micropaleontol. 22, 3–15.
Kaboth, S., Bahr, A., Reichart, G.J., Jacobs, B., Lourens, L.J., 2015. New insights into upper MOW variability over the last 150 kyr from IODP 339 Site U1386 in the Gulf of Cadiz. Mar. Geol. 377, 136–145. https://doi.org/10.1016/j.margeo.2015.08.014.
Kuhlemann, J., Rohling, E.J., Krumrei, I., Kubik, P., Ivy-Ochs, S., Kucera, M., 2008. Regional synthesis of Mediterranean atmospheric circulation during the last Glacial Maximum. Science 321, 1338–1340. https://doi.org/10.1126/science.1157638.
Kuhlmann, J., Asioli, A., Trincardi, F., Klügel, A., Huhn, K., 2015. Sedimentary response to Milankovitch-type climatic oscillations and formation of sediment undulations: evidence from a shallow-shelf setting at Gela Basin on the Sicilian continental margin. Quat. Sci. Rev. 108, 76–94. https://doi.org/10.2016/j.quascirev.2014.10.030.
Kuhlmann, J., Asioli, A., Trincardi, F., Klügel, A., Huhn, K., 2017. Landslide frequency and failure mechanisms at NE Gela Basin (Strait of sicily). J. Geophys. Res. Sol. Ea. 122, 2223–2243. https://doi.org/10.1002/2017JF004251.
Lambeck, K., Rouby, H., Purcell, A., Sun, Y., Sambridge, M., 2014. Sea level and global ice volumes from the last Glacial Maximum to the Holocene. Proc. Natl. Acad. Sci. 111 (43), 15296–15303. https://doi.org/10.1073/pnas.1411762111.
Lebreiro, S.M., Antón, L., Reguera, I., Marzocchi, A., 2018. Paleoceanographic and climatic implications of a new Mediterranean Outflow branch in the southern Gulf of Cadiz. Quat. Sci. Rev. 197, 92–111. https://doi.org/10.1016/j.quascirev.2018.07.036.
Lee, H.J., 2009. Timing of occurrence of large submarine landslides on the Atlantic Ocean margin. Mar. Geol. 264, 53–64. https://doi.org/10.1016/j.margeo.2008.09.009.
Lermusiaux, P.F.J., Robinson, A.R., 2001. Features of dominant mesoscale variability, circulation patterns and dynamics in the Strait of Sicily. Deep Sea Res. Part I Oceanogr. Res. Pap. 48, 1953–1997. https://doi.org/10.1016/S0967-0637(00)00114-X.
Lirer, F., Sprovieri, M., Ferraro, L., Vallefuoco, M., Capotondi, L., Cascella, A., Petrosino, P., Insinga, D.D., Pelosi, N., Tamburrino, S., Lubritto, C., 2013. Integrated stratigraphy for the Late Quaternary in the eastern Tyrrhenian Sea. Quat. Int. 292, 71–85. https://doi.org/10.1016/j.quaint.2012.08.2055.
Ma, X., Yan, J., Hou, Y., Lin, F., Zheng, X., 2016. Footprints of obliquely incident internal solitary waves and internal tides near the shelf break in the northern South China Sea. J. Geophys. Res. Ocean. 121, 6762–6778. https://doi.org/10.1002/2016JC012009.
Martín-Chivelet, J., Fregenal-Martínez, M.A., Chacón, B., 2008. Traction Structures in Contourites. Dev. Sedimentol. 60, 159–182. https://doi.org/10.1016/S0070-4571(08)10010-3.
Martinez-Ruiz, F., Kastner, M., Gallego-Torres, D., Rodrigo-Gámiz, M., Nieto-Moreno, V., Ortega-Huertas, M., 2015. Paleoclimate and paleoceanography over the past 20,000 yr in the Mediterranean Sea Basins as indicated by sediment elemental proxies. Quat. Sci. Rev. 107, 25–46. https://doi.org/10.1016/j.quascirev.2014.09.018.
Martorelli, E., Petroni, G., Chiocci, F.L., Pantelleria Sci, P., 2011. Contourites offshore Pantelleria Island (Sicily Channel, Mediterranean Sea): depositional, erosional and biogenic elements. Geo-Mar. Lett. 31, 481–493. https://doi.org/10.1007/s00367-011-0244-0.
Martorelli, E., Bosman, A., Casalbore, D., Falcini, F., 2016. Interaction of down-slope and along-slope processes off Capo Vaticano (southern Tyrrhenian Sea, Italy), with particular reference to contourite-related landslides. Mar. Geol. 378, 43–55. https://doi.org/10.1016/j.margeo.2016.01.005.
Massé, L., Faugères, J.C., Hrovatin, V., 1998. The interplay between turbidity and contour current processes on the Columbia Channel fan drift, Southern Brazil Basin. Sediment. Geol. 115, 111–132. https://doi.org/10.1016/S0037-0738(97)00089-4.
McCave, I.N., Andrews, J.T., 2019. Distinguishing current effects in sediments delivered to the ocean by ice. I. Principles, methods and examples. Quat. Sci. Rev. 212, 92–107. https://doi.org/10.1016/j.quascirev.2019.03.031.
McCave, I.N., Hall, I.R., 2006. Size sorting in marine muds: processes, pitfalls, and prospects for paleoflow-speed proxies. Geochem. Geophys. Geosyst. 7 (10) https://doi.org/10.1029/2006GC001284.
McCave, I.N., Manighetti, B., Robinson, S.G., 1995. Sortable silt and fine sediment size/composition slicing: parameters for paleocurrent speed and paleoceanography. Paleoceanogr. Paleoclim. 10, 593–610. https://doi.org/10.1029/94PA03039.
McCave, I.N., Thornalley, D.J.R., Hall, I.R., 2017. Relation of sortable silt grain-size to deep-sea current speeds: calibration of the 'Mud Current Meter'. Deep Sea Res. Oceanogr. Res. Pap. 127, 1–12. https://doi.org/10.1016/j.dsr.2017.07.003.
McCulloch, M., Taviani, M., Montagna, P., Lopez Correa, M., Remia, A., Mortimer, G., 2010. Proliferation and demise of deep-sea corals in the Mediterranean during the Younger Dryas. Earth Planet. Sci. Lett. 298, 143–152. https://doi.org/10.1016/j.epsl.2010.07.036.
McNeill, L.C., Shillington, D.J., Carter, G.D.O., Everest, J.D., Gawthorpe, R.L., Miller, C., Phillips, M.P., Collier, R.E.L., Cvetkoska, A., De Gelder, G., Diz, P., Doan, M.L., Ford, M., Geraga, M., Gillespie, J., Hemelsdaël, R., Herrero-Bervera, E., Ismaiel, M., Janikian, L., Kouli, K., Le Ber, E., Li, S., Maffione, M., Mahoney, C., Machlus, M.L., Michas, G., Nixon, C.W., Oflaz, S.A., Omale, A.P., Panagiotopoulos, K., Pechlivanidou, S., Sauer, S., Seguin, J., Sergiou, S., Zakharova, N.V., Green, S., 2019. High-resolution record reveals climate-driven environmental and sedimentary changes in an active rift. Sci. Rep. 9, 1–11. https://doi.org/10.1038/s41598-019-40022-w.
Melki, T., Kallel, N., Jorrissen, F.J., Guichard, F., Dennielou, B., Berné, S., Labeyrie, L., Fontugne, M., 1999. Abrupt climate change, sea surface salinity and

paleoproductivity in theWestern Mediterranean (Gulf of Lion) during the last 28 kyr. Palaeogeogr. Palaeoclimatol. Palaeocol. 279, 96–113. https://doi.org/10.1016/j.palaeo.2009.05.005.
Milliman, J., Farnsworth, K., 2011. River Discharge to the Coastal Ocean: A Global Synthesis. Cambridge University Press, p. 24. https://doi.org/10.1017/CBO9780511781247.
Millot, C., 1999. Circulation in the Western Mediterranean Sea. J. Mar. Syst. 20 (1–4), 423–442. https://doi.org/10.1016/S0924-7963(98)00078-5.
Millot, C., Taupier-Letage, I., 2005. Circulation in the Mediterranean Sea. In: Saliot, A. (Ed.), The Mediterranean Sea. Springer Berlin Heidelberg, Berlin, Heidelberg, pp. 29–66. https://doi.org/10.1007/b107143.
Minisini, D., Trincardi, F., 2009. Frequent failure of the continental slope: the Gela Basin (sicily channel). J. Geophys. Res. Earth 114, 1–17. https://doi.org/10.1029/2008JF001037.
Minisini, D., Trincardi, F., Asioli, A., Canu, M., Foglini, F., 2007. Morphologic variability of exposed mass-transport deposits on the eastern slope of Gela Basin (Sicily channel). Bas. Res. 19, 217–240. https://doi.org/10.1111/j.1365-2117.2007.00324.x.
Miramontes, E., Cattaneo, A., Jouet, G., Théreau, E., Thomas, Y., Rovere, M., Cauquil, E., Trincardi, F., 2016. The Pianosa Contourite Depositional System (Northern Tyrrhenian Sea): drift morphology and Plio-Quaternary stratigraphic evolution. Mar. Geol. 378, 20–42. https://doi.org/10.1016/j.margeo.2015.11.004.
Miramontes, E., Eggenhuisen, J.T., Jacinto, R.S., Poneti, G., Pohl, F., Normandeau, A., Campbell, D.C., Hernández-Molina, F.J., 2020. Channel-levee evolution in combined contour current–turbidity current flows from flume-tank experiments. Geology 48 (4), 353–357. https://doi.org/10.1130/G47111.1.
Mix, A.C., Bard, E., Schneider, R., 2001. Environmental processes of the ice age: Land, oceans, glaciers (EPILOG). Quat. Sci. Rev. 20, 627–657. https://doi.org/10.1016/S0277-3791(00)00145-1.
Mulder, T., Syvitski, J.P.M., Migeon, S., Faugères, J.C., Savoye, B., 2003. Marine hyperpycnal flows: Initiation, behaviour and related deposits. A review. Mar. Pet. Geol. 20, 861–882. https://doi.org/10.1016/j.marpetgeo.2003.01.003.
Mulder, T., Faugères, J.-T., Gonthier, E., 2008. Mixed turbidite-contourite systems. In: Rebesco, M., Camerlenghi, A. (Eds.), Contourites. Developments in Sedimentology 60. Elsevier, pp. 435–456. https://doi.org/10.1016/S0070-4571(08)10021-8.
Pedrosa-Pàmies, R., Parinos, C., Sanchez-Vidal, A., Gogou, A., Calafat, A., Canals, M., Bouloubassi, I., Lampadariou, N., 2015. Composition and sources of sedimentary organic matter in the deep eastern Mediterranean Sea. Biogeosciences 12, 7379–7402. https://doi.org/10.5194/bg-12-7379-2015.
Pellegrini, C., Maselli, V., Trincardi, F., 2016. Pliocene–Quaternary contourite depositional system along the south-western Adriatic margin: changes in sedimentary stacking pattern and associated bottom currents. Geo-Marine Lett. 36, 67–79. https://doi.org/10.1007/s00367-015-0424-4.
Perez-Folgado, M., Sierro, F.J., Flores, J.A., Cacho, I., Grimalt, J.O., Zahn, R., Shackleton, N., 2003. Western Mediterranean planktonic foraminifera events and millennial climatic variability during the last 70 kyr. Mar. Micropaleontol. 48, 49–70. https://doi.org/10.1016/S0377-8398(02)00160-3.
Petrovic, A., Lantzsch, H., Schenk, T., Marquardt, J., Tischack, J., Hanebuth, T.J.J., 2019. Post-LGM upward shift of the Mediterranean Outflow Water recorded in a contourite drift off NW Spain. Mar. Geol. 407, 334–379. https://doi.org/10.1016/j.margeo.2018.11.015.
Piva, A., Asioli, A., Schneider, R.R., Trincardi, F., Andersen, N., Colmenero-Hidalgo, E., Dennielou, B., Flores, J.-A., Vigliotti, L., 2008. Climatic cycles as expressed in sediments of the PROMESS1 borehole PRAD1–2, central Adriatic, for the last 370 ka: 1. Integrated stratigraphy. Geochem. Geophys. Geosyst. 9, Q01R01 https://doi.org/10.1029/2007GC001713.
Potter, P.E., Maynard, J.B., Depetris, P.J., 2005. Mud and Mudstones. Springer-Verlag, Berlin Heidelberg.
Pujol, C., Vergnaud-Grazzini, C., 1995. Distribution patterns of live planktic foraminifers as related to regional hydrography and productive systems of the Mediterranean Sea. Mar. Micropaleontol. 25, 187–217. https://doi.org/10.1016/0377-8398(95)00002-I.
Rebesco, M., Hernández-Molina, F.J., Van Rooij, D., Wåhlin, A., 2014. Contourites and associated sediments controlled by deep-water circulation processes: State-of-the-art and future considerations. Mar. Geol. 352, 111–154. https://doi.org/10.1016/j.margeo.2014.03.011.
Reimer, P.J., Bard, E., Bayliss, A., Beck, J.W., Blackwell, P.G., Bronk Ramsey, C., Buck, C. E., Cheng, H., Edwards, R.L., Friedrich, M., Grootes, P.M., Guilderson, T.P., Haflidason, H., Hajdas, I., Hatté, C., Heaton, T.J., Hogg, A.G., Hughen, K.A., Kaiser, K.F., Kromer, B., Manning, S.W., Niu, M., Reimer, R.W., Richards, D.A., Scott, E.M., Southon, J.R., Turney, C.S.M., van der Plicht, J., 2013. IntCal13 and MARINE13 radiocarbon age calibration curves 0-50000 years cal BP. Radiocarbon 55 (4), 1869–1887. https://doi.org/10.2458/azu_js_rc.55.16947.
Revel, M., Ducassou, E., Skonieczny, C., Colin, C., Bastian, L., Bocsh, D., Migeon, S., Mascle, J., 2015. 20,000 years of Nile River dynamics and environmental changes in the Nile catchment area as inferred from Nile upper continental slope sediments. Quat. Sci. Rev. 130, 200–221. https://doi.org/10.1016/j.quascirev.2015.10.030.
Ricketts, B.D., Evenchick, C., 1999. Shelfbreak gullies; products of sea-level lowstand and sediment failure: examples from Bowser Basin, northern British Columbia. J. Sediment. Res. 69 (6), 1232–1240. https://doi.org/10.2110/jsr.69.1232.
Rogerson, M., Cacho, I., Jimenez-Espejo, F., Reguera, M.I., Sierro, F.J., Martinez-Ruiz, F., Frigola, J., Canals, M., 2008. A dynamic explanation for the origin of the western Mediterranean organic-rich layers. Geochem. Geophys. Geosyst. 9, Q07U01 https://doi.org/10.1029/2007GC001936.
Rogerson, M., Rohling, E.J., Bigg, G.R., Ramirez, J., 2012. Paleoceanography of the Atlantic-Mediterranean exchange: overview and first quantitative assessment of climatic forcing. Rev. Geophys. 50, RG2003 https://doi.org/10.1029/2011RG000376.
Rohling, E., Marino, G., Grant, K.M., 2015. Mediterranean climate and oceanography, and the periodic development of anoxic events (sapropels). Earth Sci. Rev. 143, 62–97. https://doi.org/10.1016/j.earscirev.2015.01.008.
Rothwell, R.G., Croudace, I.W., 2015. Twenty years of XRF Core Scanning Marine Sediments: What do Geochemical Proxies tell Us? In: Croudace, I.W., Rothwell, R.G. (Eds.), Micro-XRF Studies of Sediment Cores, Dev. Paleoenvironmental. Res., Vol. 17, pp. 25–103. https://doi.org/10.1007/978-94-017-9849-5_2.
Rouis-Zargouni, I., Turon, J.L., Londeix, L., Essallami, L., Kallel, N., Sicre, M.A., 2010. Environmental and climatic changes in the Central Mediterranean Sea (Siculo-Tunisian Strait) during the last 30 ka based on dinoflagellate cyst and planktonic foraminifera assemblages. Palaeogeogr. Palaeoclimatol. Palaeoecol. 285, 17–29. https://doi.org/10.1016/j.palaeo.2009.10.015.
Rovere, M., Pellegrini, C., Chiggiato, J., Campiani, E., Trincardi, F., 2019. Impact of dense bottom water on a continental shelf: an example from the SW Adriatic margin. Mar. Geol. 408, 123–143. https://doi.org/10.1016/j.margeo.2018.12.002.
Sammari, C., Millot, C., Taupier-Letage, I., Stefani, A., Brahim, M., 1999. Hydrological characteristics in the Tunisia–Sardinia–Sicily area during spring 1995. Deep Sea Res. Part I Oceanogr. Res. Pap. 46, 1671–1703. https://doi.org/10.1016/S0967-0637(99)00026-6.
Schmiedl, G., Kuhnt, T., Ehrmann, W., Emeis, K.C., Hamann, Y., Kotthoff, U., Dulski, P., Pross, J., 2010. Climatic forcing of Eastern Mediterranean deep-water formation and benthic ecosystems during the past 22,000 years. Quat. Sci. Rev. 29, 3006–3020. https://doi.org/10.1016/j.quascirev.2010.07.002.
Shanahan, T.M., McKay, N.P., Hughen, K.A., Overpeck, J.T., Otto-Bliesner, B., Heil, C.W., King, J., Scholz, C.A., Peck, J., 2015. The time-transgressive termination of the African Humid period. Nat. Geosci. 8, 140–144. https://doi.org/10.1038/NGEO2329.
Shipboard Scientific Party, 1996. Site 963. In: Emeis, K.-C., Robertson, A.H.F., Richter, C., et al. (Eds.), Proceedings of the Ocean Drilling Program, Initial Reports. 160. Texas A&M University, Houston, Texas, pp. 55–84. https://doi.org/10.2973/odp.proc.ir.160.104.1996.
Siani, G., Paterne, M., Arnold, M., Bard, E., Métivier, B., Tisnerat, N., Bassinot, F., 2000. Radiocarbon reservoir ages in the Mediterranean Sea and Black Sea. Radiocarbon 42, 271–280. https://doi.org/10.1017/S0033822200059075.
Siani, G., Paterne, M., Colin, C., 2010. Late glacial to Holocene planktic foraminifera bioevents and climatic record in the South Adriatic Sea. J. Quat. Sci. 25 (5), 808–821. https://doi.org/10.1002/jqs.1360.
Sierro, F.J., Hodell, D.A., Curtis, J., Flores, J.A., Reguera, I., Colmenero-Hidalgo, E., Barcena, M.A., Grimalt, J., Canals, M., 2005. Impact of iceberg melting during Heinrich events on Mediterranean thermohaline circulation. Paleoceanography 20, PA2019. https://doi.org/10.1029/2004PA001051.
Sprovieri, R., Di Stefano, E., Incarbona, A., Gargano, M.E., 2003. A high-resolution record of the last deglaciation in the Sicily Channel based on foraminifera and calcareous nannofossil quantitative distribution. Palaeogeogr. Palaeoclimatol. Palaeoecol. 202, 119–142. https://doi.org/10.1016/S0031-0182(03)00632-1.
Stanford, J.D., Hemingway, R., Rohling, E.J., Challenor, P.G., Medina-Elizalde, M., Lester, A.J., 2011. Sea-level probability for the last deglaciation: a statistical analysis of far-field records. Glob. Planet. Change 79, 193–203. https://doi.org/10.1016/j.gloplacha.2010.11.002.
Stow, D., Smillie, Z., 2020. Distinguishing between deep-water sediment facies: Turbidites, contourites and hemipelagites. Geosci. 10 https://doi.org/10.3390/geosciences10020068.
Stuiver, M., Reimer, P.J., 1993. Extended ^{14}C database and revised CALIB radiocarbon calibration program. Radiocarbon 35, 215–230. https://doi.org/10.1017/S0033822200013904.
Tesi, T., Miserocchi, S., Goni, M., Langone, L., 2007. Source, transport and fate of terrestrial organic carbon on the western Mediterranean Sea, Gulf of Lions, France. Mar. Chem. 105, 101–117. https://doi.org/10.1016/j.marchem.2007.01.005.
Tesi, T., Asioli, A., Minisini, D., Maselli, V., Dalla Valle, G., Gamberi, F., Langone, L., Cattaneo, A., Montagna, P., Trincardi, F., 2017. Large-scale response of the Eastern Mediterranean thermohaline circulation to African monsoon intensification during sapropel S1 formation. Quat. Sci. Rev. 159, 139–154. https://doi.org/10.1016/j.quascirev.2017.01.020.
Tjallingii, R., Röhl, U., Kölling, M., Bickert, T., 2007. Influence of the water content on X-ray fluorescence core-scanning measurements in soft marine sediments. Geochem. Geophys. Geosyst. 8, Q02004 https://doi.org/10.1029/2006GC001393.
Toucanne, S., Jouet, G., Ducassou, E., Bassetti, M.-A., Dennielou, B., Angue Minto'o, C. M., Lahmi, M., Touyet, N., Charlier, K., Lericolais, G., Mulder, T., 2012. A 130,000-year record of Levantine Intermediate Water flow variability in the Corsica Trough, western Mediterranean Sea. Quat. Sci. Rev. 33, 55–73. https://doi.org/10.1016/j.quascirev.2011.11.020.
Van Rooij, D., Iglesias, J., Hernández-Molina, F.J., Ercilla, G., Gomez-Ballesteros, M., Casas, D., Llave, E., De Hauwere, A., Garcia-Gil, S., Acosta, J., Henriet, J.P., 2010. The Le Danois Contourite Depositional System: Interactions between the Mediterranean Outflow Water and the upper Cantabrian slope (North Iberian margin). Mar. Geol. 274, 1–20. https://doi.org/10.1016/j.margeo.2010.03.001.
Verdicchio, G., Trincardi, F., 2008. Mediterranean shelf-edge muddy contourites: examples from the Gela and South Adriatic basins. Geo-Mar. Lett. 28, 137–151. https://doi.org/10.1007/s00367-007-0096-9.
Vergnaud-Grazzini, C., Devaux, M., Znaidi, J., 1986. Stable isotope "anomalies" in Mediterranean Pleistocene records. Mar. Micropaleontol. 10, 35–69. https://doi.org/10.1016/0377-8398(86)90024-1.
Vergnaud-Grazzini, C., Borsetti, A.M., Cati, F., Colantoni, P., D'Onofrio, S., Saliège, J.F., Sartori, R., Tampieri, R., 1988. Paleoceanographic record of the last deglaciation in

the Strait of Sicily. Mar. Micropaleontol. 13, 1–21. https://doi.org/10.1016/0377-8398(88)90010-2.

Vigliotti, L., Verosub, K.L., Cattaneo, A., Trincardi, F., Asioli, A., Piva, A., 2008. Palaeomagnetic and rock magnetic analysis of Holocene deposits from the Adriatic Sea: Detecting and dating short-term fluctuations in sediment supply. The Holocene 18 (1), 141–152. https://doi.org/10.1177/0959683607085605.

Vizzini, S., Sarà, G., Mateo, M.A., Mazzola, A., 2003. $\delta^{13}C$ and $\delta^{15}N$ variability in *Posidonia oceanica* associated with seasonality and plant fraction. Aquat. Bot. 76 (3), 195–202. https://doi.org/10.1016/S0304-3770(03)00052-4.

Voigt, I., Chiessi, C., Piola, A., Henrich, R., 2016. Holocene changes in Antarctic Intermediate Water flow strength in the Southwest Atlantic. Palaeogeogr. Palaeoclimatol. Palaeoecol. 463, 60–67. https://doi.org/10.1016/j.palaeo.2016.09.018.

Wang, M., Zheng, H., Xie, X., Fan, D., Yang, S., Zhoa, Q., Wang, K., 2011. A 600-year flood history in the Yangtze River drainage: comparison between a subaqueous delta and historical records. Chin. Sci. Bull. 56, 188–195. https://doi.org/10.1007/s11434-010-4212-2.

Zaniboni, F., Pagnoni, G., Paparo, M.A., Gauchery, T., Rovere, M., Argnani, A., Armigliato, A., Tinti, S., 2021. Tsunamis from Submarine Collapses along the Eastern Slope of the Gela Basin (Strait of Sicily). Front. Earth Sci. 8, 602171. https://doi.org/10.3389/feart.2020.602171.